About the role of the hydrogen during stress corrosion cracking of a low-copper Al-Zn-Mg alloy

Loïc Oger, Eric Andrieu, Grégory Odemer, Lionel Peguet, Christine Blanc

Version of Record: https://www.sciencedirect.com/science/article/pii/S0925838821048015
Manuscript_6ea63b86bd68f47dce5cd43bc9efecb3

About the role of the hydrogen during stress corrosion cracking of a low-copper Al-Zn-Mg alloy

L. Oger[1], E. Andrieu[1], G. Odemer[1], L. Peguet[2] and C. Blanc[1,*]

[1] CIRIMAT, Université de Toulouse, CNRS, INP-ENSIACET, 4 Allée Emile Monso, BP 44362, 31030 Toulouse Cedex 4, France

[2] Constellium Technology Center, 725 rue Aristide Bergès, CS 10027, 38341 Voreppe cedex, France

[*] Corresponding author. Tel./fax: +33 (0)5 34 32 34 07 / +33 (0)5 34 32 34 98

*E-mail addres*s: christine.blanc@ensiacet.fr.

Abstract - This study provides some clarifications about the influence of microstructural parameters on the susceptibility of low-copper Al-Zn-Mg alloy to stress corrosion cracking (SCC). Tensile tests in air were carried out on AA7046 in T4 and T4 aged at 150 °C (named 150/20) metallurgical states after pre-exposure of the specimens to a chloride solution under mechanical loading. The results showed the predominant role of the corrosion-induced hydrogen during SCC process on the loss of elongation to failure. Scanning kelvin probe force microscopy (SKPFM) measurements were performed for the T4 specimens as well as for a 530 °C heat-treated T4 specimen with a coarse-grained microstructure; this allowed the contribution of hydrogen diffusion at the grain boundaries on the hydrogen distribution to be highlighted. The analysis of the fracture modes after tensile tests and hydrogen diffusion profiles obtained by SKPFM in the framework of previous studies investigating the microstructure-hydrogen and plasticity-hydrogen relationships allowed to propose a qualitative model to describe SCC phenomena. The detrimental role of hydrogen at the grain boundaries on the mechanical behaviour was highlighted; the outcome of the evaluation of

results from the present study in combination with our previous studies and literature data suggested that it can be limited by hydrogen trapping on intragranular η-$MgZn_2$ precipitates.

Keywords: metals and alloys; corrosion; mechanical properties; diffusion; dislocations and disclinations; grain boundaries.

1. Introduction

Today, environmental issues are at the heart of the industrial policies of all sectors as this is the case for the automotive industry. Especially in the European Union, standards requiring a drastic reduction in fuel consumption and carbon dioxide emissions compel the industry to redesign their vehicles [1]. As an answer to this challenge, during the last decades, efforts focused on reduced-weight vehicles, which led to double the average amount of aluminium in cars [2]. Aluminium alloys, e.g. 5xxx (Al-Mg) and 6xxx (Al-Mg-Si) series are widely used as they offer a good ratio between mechanical properties, formability and corrosion resistance. However, their maximal yield stress (YS) is too low to use them for the most demanding structural parts, which remains a current challenge [3].

One solution consists in using precipitation-hardening 7xxx (Al-Zn-Mg (-Cu)) alloys, known to have the highest mechanical properties among aluminium alloys. However, in their peak-aged state, they can be susceptible to stress corrosion cracking (SCC), which depends on their composition and processing parameters [4–6]. Damage observed during SCC is attributed to two main phenomena, i.e. crack propagation assisted by anodic dissolution [7] and hydrogen-enhanced SCC [7-9]. Although a synergy of both is assumed to be responsible for the loss of mechanical properties, the major contribution of the hydrogen to explain the SCC of both low- and high-copper 7xxx alloys is increasingly acknowledged [7,10–14].

The hydrogen produced during the corrosion processes in relation with metallurgical heterogeneities can diffuse through interstitial sites and be trapped in sites where its chemical potential is lowered as suggested by literature related to steel [15–17]. Among the trapping sites, some are reversible like dislocations [18], vacancies [19] and low-angle grain boundaries, whereas others are irreversible like precipitates [20] or high-angle grain boundaries [21,22]. The uptake of hydrogen in aluminium alloys has been strongly demonstrated to be related to a decrease in the elongation to failure and to changes in the

fracture modes [7,23]. Hydrogen-charged zones are generally characterized by brittle inter- and intragranular fracture [24]. This can be observed even without macroscopically visible corrosion attack, as suggested by studies focused on cathodically hydrogen charged samples [16,25] or in water vapor [5,10]. However, the understanding of the specific role of the hydrogen remains a major issue for metallurgical optimization. For some authors, the loss of mechanical properties would be associated with hydrogen dissolved within the lattice leading to atomic decohesion [20,26], whereas others discussed the critical role of hydrogen-dislocation interactions and the role of hydrogen trapped at the grain boundaries [25,27]. Many models, e.g. HELP (Hydrogen-Enhanced Localized Plasticity), HEDE (Hydrogen-Enhanced DEcohesion) or AIDE (Adsorption-Induced Dislocation Emission) [28], resulted from all these hypotheses and were regularly questioned. So far there is no conclusive evidence that any one particular model among those proposed in the literature is more relevant than all of the others to explain the hydrogen-microstructure interactions and their consequences on the material behavior. Nevertheless, numerous works tend to assert that the hydrogen embrittlement is due to the influence of the hydrogen on plasticity [29–32]. However, only few studies bring experimental evidences based on hydrogen amount measurements or localization to demonstrate the relationship between SCC and hydrogen.

The present work follows a series of articles aiming to clarify the influence of specific microstructural parameters, namely the η-$MgZn_2$ precipitates and dislocations on hydrogen diffusion and trapping [25,33,34]. In these previous works, the specific case of the AA7046 was studied due to its low copper content leading to a low susceptibility to intergranular corrosion, which allows the specific role of the hydrogen to be highlighted. It has been demonstrated that the hydrogen in the AA7046-T4 led to brittle transgranular and intergranular fracture. The use of Scanning Kelvin Probe Force Microscopy (SKPFM) allowed to localize the hydrogen and to demonstrate the relationship between the brittle areas

observed and high concentrations of hydrogen at the grain boundaries. After 20 hours of heat treatment at 150 °C, in the 150/20 state, the susceptibility of the alloy was significantly lowered which was attributed to hydrogen trapping at the intragranular η-$MgZn_2$ precipitates [25]. Works on cold worked specimens also showed interactions of hydrogen with the dislocation network which acted as short-circuit diffusion paths [33]. Finally, it was also shown that the hydrogen could be transported by the dislocations during the deformation processes [34].

The present work completes the previous results; its aim is to detail the effects of hydrogen on the fracture modes and on the mechanical properties as a function of the alloy microstructure by performing SCC tests in a chloride solution on AA7046 in two metallurgical states, i.e. T4 and 150/20. The microstructure of the samples was characterized by transmission electron microscopy (TEM) in a previous work [25]; only the main results are given here in the experimental section. The samples were exposed under stress in the corrosive environment for different durations, and then tested by tensile tests at 10^{-3} s^{-1} in air. The specific role of the hydrogen was investigated by performing optical microscope (OM) observations of the corrosion defects and scanning electron microscope (SEM) observations of the fracture surfaces. The loss of mechanical properties has been related to the hydrogen amounts measured by a melting method. The diffusion of the hydrogen at the grain boundaries was investigated by elaborating a third metallurgical state referred to as T4b and corresponding to a larger-grain microstructure. The hydrogen penetration depth in the T4b state was compared to that of the T4 state already analyzed in a previous work [25]. The outcome of the evaluation of results from the present study in combination with our previous studies and literature data allowed to propose a global mechanism to explain the SCC susceptibility of the AA7046.

2. Materials and experimental procedure

a. Materials description and specimen preparation

The AA7046 (6.6-7.6 wt.% Zn, 1.0-1.6 wt.% Mg, <0.2 wt.% Cu) was examined in the present study as 2-mm thick sheets in three different metallurgical states. The reference state, called T4, was homogenized, hot rolled, cold rolled and then solution heat treated and stored at room temperature to reach a substantially stable state. Two other states, named 150/20 and T4b were obtained from the reference state:

- The 150/20 state was obtained by a heat treatment at 150 °C for 20 hours to allow the formation of intragranular η-$MgZn_2$ precipitates;
- The T4b state was obtained by a heat treatment at 530 °C for 48 hours to allow grain growth, followed by a quenching for 8 minutes in water at 25 °C.

The stability of the microstructures was verified by Vickers hardness measurements performed daily during 2 weeks following the heat treatments.

The microstructure of the T4 and 150/20 states were fully detailed in our previous work [25] and will thus only be briefly summarized:

- AA7046-T4 had a recrystallized microstructure with an average grain size of 25 µm. Coarse intermetallic precipitates, smaller than 10 µm, were identified as Al_3Fe and Ti_3Al by energy dispersive X-ray spectroscopy (EDX). TEM observations highlighted the presence of spherical Al_3Zr dispersoids of approximately 40 nm diameter. Intergranular $MgZn_2$ precipitates were also observed. The presence of Guinier-Preston zones was highly suspected due to the long-term (>2 years) storage, even if they had not been directly observed.
- The heat treatment applied to reach the 150/20 state did not affect the grain size, the coarse precipitates and the dispersoids, but led to the formation of intragranular η-$MgZn_2$ precipitates. No hardening was measured due to the

size of the intragranular precipitates (152 ± 2 HV and 150 ± 3 HV for T4 and 150/20 specimens, respectively). A noticeable coarsening of the intergranular precipitates (15 nm for T4 to 60 nm for 150/20) was also observed, accompanied by the growth of a precipitate free zone (PFZ) of approximately 120 nm.

For all experiments performed in this study, samples were cut from the sheets and were mechanically ground with abrasive paper SiC 1200 and then polished with diamond paste from 9 to 1 μm. During the abrading and polishing steps, only distilled water was used as lubricant. Finally, samples were cleaned with water in ultrasonic bath for a maximal duration of 30 seconds to limit hydrogen penetration as shown by Birnbaum *et al.* [16].

b. Microstructural examination

As described above, the microstructures of the T4 and 150/20 states of the AA7046 were already characterized at different scales in previous studies [25]. Here, only strategic complementary images will be presented for these states, and only the T4b state especially manufactured for this study was deeply investigated. Samples of this last state were observed by polarized light microscopy after etching for 90 s in HBF_4 under an imposed potential of 30 V. The average grain size was then estimated by the linear intercept method. Microhardness measurements were carried out by indentation on a *BUEHLER-Omnimet 2100* tester. A load of 500 g was chosen to provide global and accurate measurements regarding the thickness of the sample and the size of the coarse precipitates.

It must be reminded that coarse and thinner precipitates in all three microstructures were deeply studied by SEM coupled with EDX and by TEM. Observations by TEM required a specific sample preparation: the sample was ground with SiC 1200 abrasive paper until a thickness of 100 μm, then cut in discs of 3 mm diameter and electropolished in a solution

(CH_3OH (900 mL) + HNO_3 (300 mL)) at -15 °C in a *TenuPol-5*. For the thinnest precipitates, high-resolution TEM (HR-TEM) imaging was performed. The images were then analyzed by Fourier Transform.

The OM used was an *Olympus PMG3*, the SEM was a *LEO435VP* coupled with an *EDS IMIX analyser* and the TEM was a *JEOL-JEM-2010* equipped with an *EDX analyser* with a spot varying from 1.5 to 30 nm.

c. Mechanical properties

Tensile test samples were machined by electro-erosion in the long transverse (LT) direction of the sheet. Tensile tests were performed at 10^{-3} s^{-1} at room temperature in ambient atmosphere for non-exposed specimens. Similar tensile tests were performed for the T4 and 150/20 states after SCC tests (see section e) to evaluate their residual mechanical properties. Due to the thickness of the sheet, a study of the SCC behavior in the short transverse (ST) direction was not feasible, while Speidel showed that hot rolled plates of high strength aluminium alloys are much more susceptible to SCC when stressed in the ST direction than in the LT and in the longitudinal (L) directions [35]. He also showed that globally the LT direction, which is the relevant stressed direction in automotive applications using cold rolled thin sheets, was more susceptible than the L direction. For each tensile test, at least three specimens were tested to ensure repeatability. The corresponding fracture surfaces were then observed by SEM to characterize the fracture modes.

d. Corrosion behavior

Corrosion experiments were carried out on electrodes made with square-shaped specimens of AA7046 cold mounted in epoxy resin to obtain a surface area of 1 cm^2 exposed to a 0.6 M NaCl solution. Only the longitudinal (L-LT) plane was exposed to the electrolyte

for both metallurgical states. Electrochemical measurements were carried out using a three-electrode system, with a platinum counter-electrode and a saturated calomel electrode (SCE) as reference. Open Circuit Potential (OCP) measurements were carried out from 15 minutes to 72 hours of exposure to the electrolyte, and the morphology of the corrosion defects was observed with an OM for each duration of exposure.

e. SCC behavior

The SCC behavior of the alloy was studied by using tensile test samples similar to those used for mechanical tests. The SCC setup consisted in a 2.6 L cell mounted on a tensile test machine with a 10 kN load cell. The tensile samples were freely let at their corrosion potential in a 0.6 M aerated chloride solution at room temperature for 1, 5, 24 and 72 hours under an imposed loading of 80 % YS. Then, a tensile test at a strain rate of 10^{-3} s^{-1} was carried out at room temperature in air. The time between the end of SCC tests and the beginning of the tensile tests was maintained constant, i.e. 15 min, in order to avoid any dispersive effect linked to a potential hydrogen desorption assumed to be negligible for such a short time. During SCC exposure, the corrosion potential of the tested samples was simultaneously measured. A three-electrode system similar to the one previously described was used in order to monitor electrochemical behavior changes.

The loss of mechanical properties after SCC exposure was measured by comparison to non-exposed samples, and it was related to the characterization of the damage. The corrosion defects morphology was observed by OM on the gauge length (L-LT) and in the short transverse (ST) direction (LT-ST plane). Changes in fracture surfaces and cracks formed on the gauge length were observed by SEM.

f. Techniques and methodology used for cathodic hydrogen pre-charging, hydrogen global content measurements and hydrogen detection

i. Measurements of the global hydrogen amount

After SCC tests, the global hydrogen amount in the samples was measured by a melting method using an analyzer G8 GALILEO. The sensitivity of this method was about 1 wppm and no vacuum was necessary, which limited hydrogen desorption. A preliminary study of the optimal sample weight and shape to be used for hydrogen measurements was performed and brought to use samples of approximately 0.3 g. The near surface of the samples was polished using a 3 μm diamond paste before the measurements in order to avoid an overestimation of the hydrogen content due to hydrogen in the hydroxide passive layer or in the corrosion products at the surface [36].

ii. Cathodic hydrogen pre-charging and local detection by SKPFM

SKPFM was used on cathodically hydrogen pre-charged samples to compare the hydrogen diffusion in AA7046 T4 (results from [25]) and T4b states. Samples of AA7046 of 15 x 4 x 2 mm^3 were cathodically charged in a pH 2 sulfuric acid solution with an imposed potential of -1.450 V/SCE for 72 hours. A three-electrode system similar to the one previously described for corrosion tests was used. The hydrogen diffusion inside the pre-charged samples was then studied by SKPFM.

As SKPFM was widely described in our previous works [25,33,37], only a short reminder is given here. The method consists in measuring the electronic output work at the alloy surface, corresponding to a surface potential quoted *V*. Several works showed that this property was modified in the presence of hydrogen in the alloy [38–40]. It was attributed to the modifications of a local electrochemical equilibrium that would exist in the thin water film formed at the alloy near surface [41]. Despite the fact that this would be driven by the desorption of diffusible hydrogen, SKPFM measurements carried out in vacuum showed that

it was possible to detect hydrogen, and our previous works demonstrated that even trapped hydrogen could be detected [25]. Therefore, it is possible to measure hydrogen penetration depth.

In this study, a *5500 Agilent* Atomic Force Microscope (AFM) was used in single pass mode (topography and surface potential simultaneously acquired). Pt-coated silicon tips were used as conductive probes. The optimal spatial resolution (approximately 50 nm) was obtained by using the Amplitude modulation (AM) – KFM mode [42]. All parameters were previously detailed [25,33,37]. All SKPFM measurements were performed at room temperature in ambient atmosphere immediately after hydrogen pre-charging. This limited hydrogen desorption, but, as previously explained, the surface potential measurements can be related to the formation of a thin water film on the samples surface depending on the relative humidity. Consequently, the surface potential measured cannot be quantitatively compared to hydrogen amounts and all measurements were normalized. ΔV was defined as the difference between the potential measured (for each depth) and the average value of the potential in the core (distance > 300 µm of the pre-charged surface) of the specimens. For this reason, only the hydrogen penetration depths measured were considered as relevant and quantitative.

After hydrogen pre-charging with the L-LT plane exposed to the sulfuric acid solution, samples were polished on the LT-ST plane with ¼ µm diamond paste, and SKPFM measurements were conducted in this plane, in the ST direction. Rectangular sections of 80 µm x 16 µm were successively scanned from the charged surface up to 400 µm in the core of the samples. An increment of 50 µm was applied with a micrometer screw between each section and all sections were then matched together to obtain a full profile. Results were analyzed with the *Gwyddion* software.

3. **Results**

a. Influence of the SCC exposure on the mechanical properties of the AA7046

Fig.1 offers a comparison of the mechanical properties of the AA7046 in T4 and 150/20 metallurgical states with and without pre-exposure to the NaCl solution. In the present study, the pre-exposure before tensile tests was always under a $0.8YS_{0.2}$ stress. A focus on stress vs strain curves for the non-exposed samples allowed to see the influence of the microstructural differences. An increase in YS values (from 364±7 MPa to 434±1 MPa) and a decrease in the elongation to failure (E_f) (from 18±1 % to 13±1 %) were noticed for the 150/20 metallurgical state by comparison to the T4 samples, which was consistent with the overall literature [27,28,43].

The stress vs strain curves were plotted after exposures of 1, 24 and 72 hours in 0.6 M NaCl under a $0.8YS_{0.2}$ loading. To make the figure easier to read, the curves obtained for 5 hours of exposure were not represented because they are similar to those obtained for 1 hour. The curves showed that the SCC pre-exposure altered the tensile properties of the alloy. Independently of the metallurgical state, no change in the elasticity domain and no decrease in the flow stress in the plasticity domain was observed. This suggested that the bearing section was not significantly affected by the corrosion defects. However, a lower elongation was obtained for all the pre-exposed samples (under sustained load) and a progressive decrease in the elongation to fracture with the duration of pre-exposure to NaCl was observed for pre-corroded samples as compared to non-exposed specimens. After 72 hours of pre-exposure, the AA7046 lost approximately 23 % in ductility in the T4 state and 15% in the 150/20 state. This suggested that the 150/20 microstructure was less susceptible to SCC than the T4 microstructure, which is consistent with existing works [7,12,28,44].

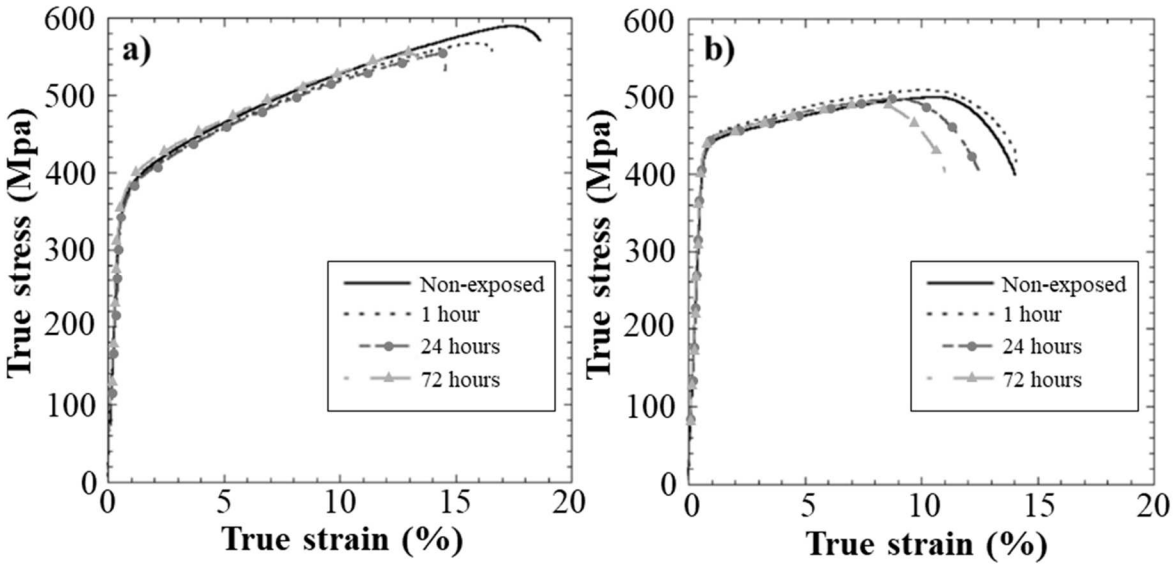

Fig. 1. True stress vs true strain curves of the AA7046 in T4 (a) and 150/20 (b) states for different SCC exposure durations.

As a complement, the fracture surfaces were observed by SEM. Observations are shown in Fig.2 for the non-exposed samples. These observations have already been described in [25], but the main results are briefly summarized here in order to allow the influence of the SCC pre-exposure to be understood:

- In the T4 state, the fracture was ductile-intergranular. The grains are clearly visible in Fig. 2a in good agreement with an intergranular fracture, but a thorough analysis revealed that the surface of the grains was covered by nano dimples (Fig. 2b), which was related to a deformation localized around η-$MgZn_2$ intergranular precipitates [45,46].
- In the 150/20 state (Fig. 2c and 2d), the fracture surface was ductile transgranular with large dimples generated by the decohesion between the matrix and the coarse intermetallic particles as well as dispersoids. Small voids were also observed; they were attributed to plastic deformation localized around intragranular precipitates, as well as around intergranular precipitates (in particular for the voids with a row shape).

In the T4 state, the AA7046 probably contains thin GP zones that could be sheared by dislocations during tensile tests. The dislocations formed during the tensile test could create a

dense network explaining the hardening with strain implement; this would also facilitate the localization of dislocations around the grain boundaries. The plastic deformation localized near intergranular precipitates should explain the ductile-intergranular fracture observed. In the 150/20 state, the fracture was ductile transgranular. This could be explained by the η-$MgZn_2$ precipitates in the grains that could be by-passed by dislocations so that the deformation was more homogeneously distributed in the grains. The differences observed could also be explained by the stress level reached in the T4 state that could lead to intergranular fracture, whereas it was too low in the 150/20 state, so that only the precipitates-matrix decohesion stress could be reached, leading to the transgranular failure mode observed.

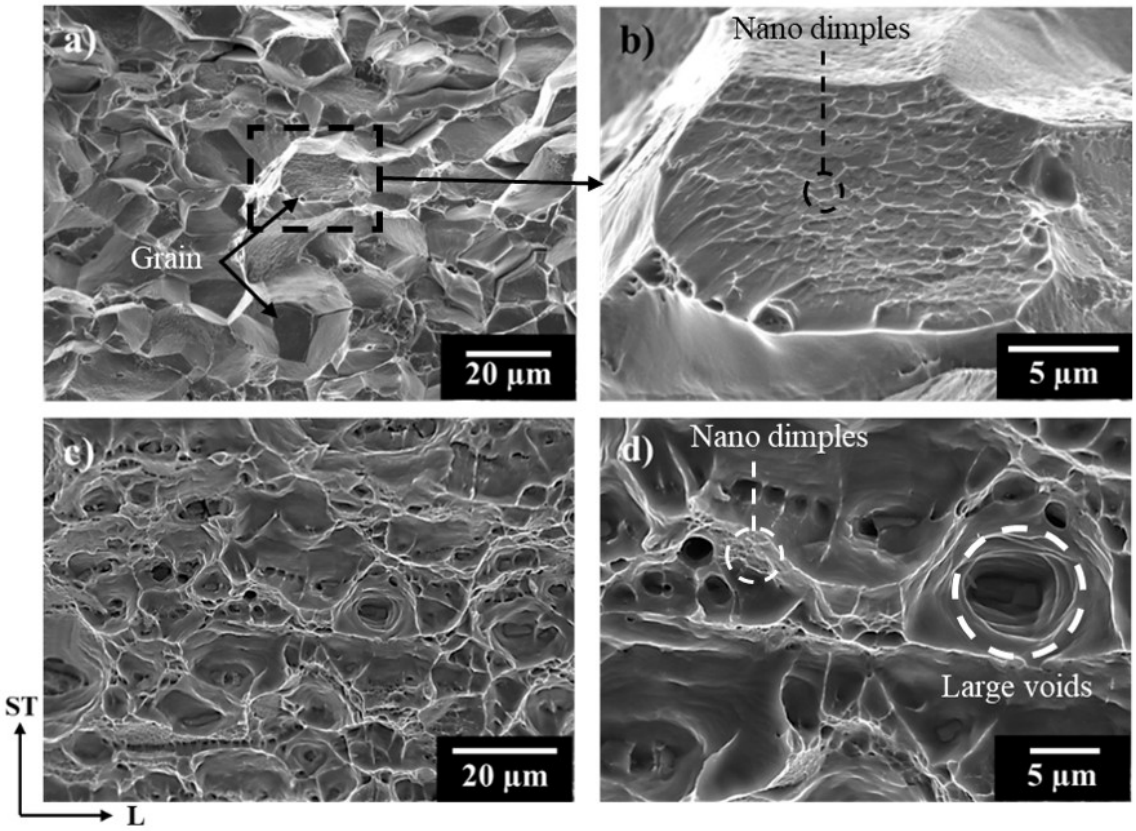

Fig. 2. SEM micrographs of the fracture surface of the non-exposed AA7046 for both metallurgical states: (a) and (b) T4 state and (c) and (d) 150/20 state. Figs. b and c adapted from Fig. 8 in [25].

Fig. 3 showed that a 72-hour pre-exposure in SCC conditions modified the fracture surfaces, in good agreement with the stress vs strain curves (Fig. 1*)*. Similar results were

obtained for the other durations of SCC tests. In the T4 state, the fracture surfaces are globally similar to those observed for non-exposed samples, except for brittle areas close to the surfaces exposed to the NaCl solution during SCC tests (Figs. 3a and 3b). All brittle zones observed were characterized by two distinct areas. At first, a brittle intergranular fracture mode close to the near surface suggested an embrittlement of the grain boundaries (Fig. 3c). Deeper in the samples, a cleavage-like fracture mode was observed surrounding the brittle intergranular areas (Fig. 3d). These brittle areas were observed up to 200 μm under the pre-exposed surface. In the 150/20 state, only few shallow quasi-cleavage areas were observed really close to the near surface (Figs. 3e and 3f). Their depth did not exceed the grain size.

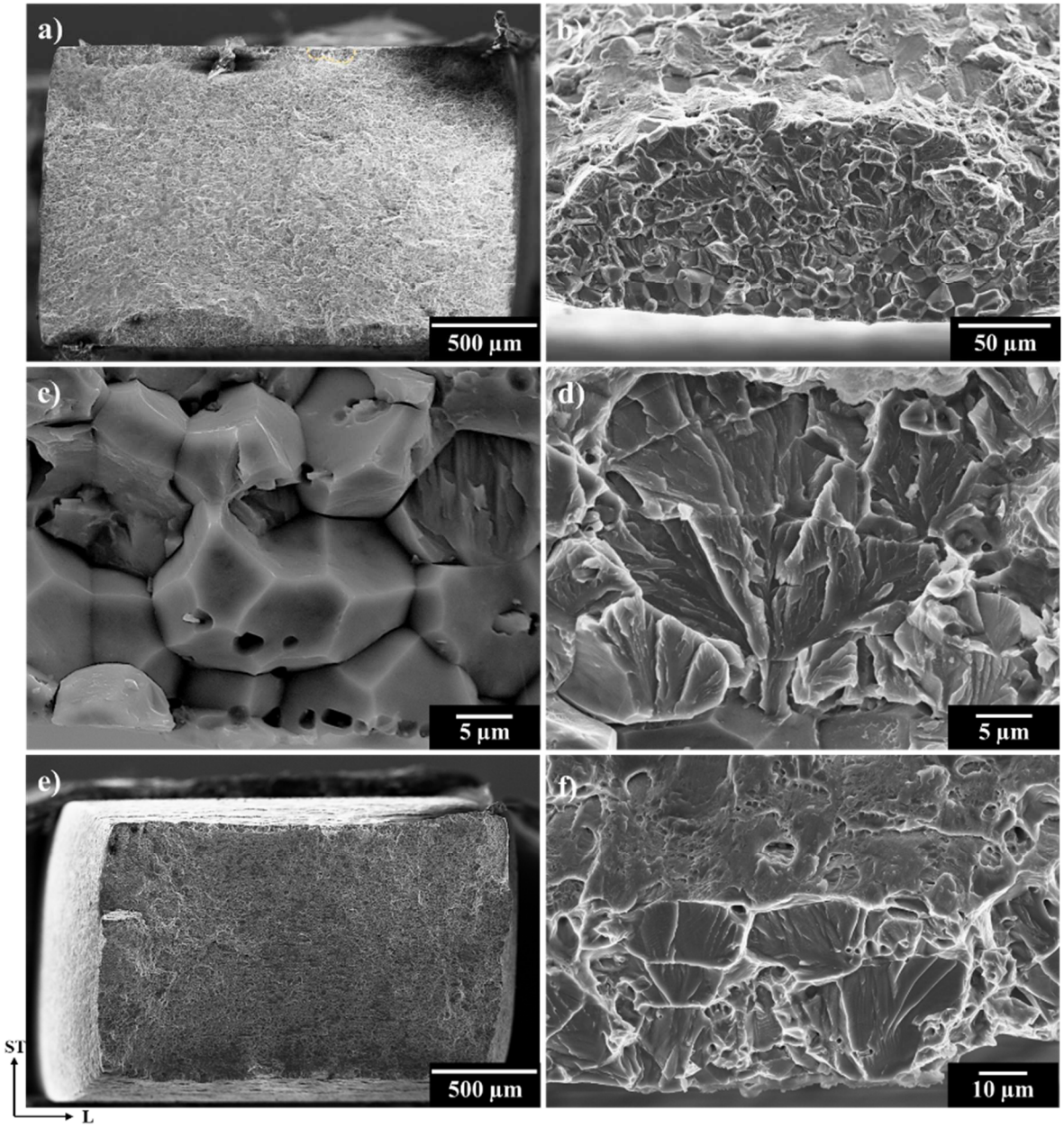

Fig. 3. SEM micrographs of the fracture surfaces of the AA7046 after SCC tests for 72 hours in 0.6 M NaCl followed by a tensile test at 10^{-3} s^{-1} in air: a) and e) show global fracture surfaces for the T4 and the 150/20 states, respectively, b) and f) show brittle fracture for the T4 and the 150/20 states, respectively, c) focus on brittle intergranular fracture and d) on brittle transgranular fracture in the T4 state.

To go further in the understanding of the SCC behaviour of the AA7046, an in-depth analysis of the damage was done. The brittle fracture surface was thoroughly characterized for all SCC pre-exposure durations; the results are summarized in Fig. 4a. For both T4 and 150/20 samples, the brittle areas extended increasingly with the exposure duration, with a more significant extension for the T4 state, which was consistent with previous SEM

observations and with the decrease in the elongation to failure previously highlighted. In these areas, failure roughly happened due to a decrease in the intergranular cohesion stress (intergranular brittle areas) or due to the high localization of plasticity (transgranular brittle areas). However, it was of interest to note that no significant difference in the damage was observed between T4 samples exposed for 24 and 72 hours to the NaCl solution. As a consequence, this criterion alone could not explain the loss of mechanical properties. Consequently, a complementary index quoted I_{SD} was defined (Eq.1) taking into account the surface damage (I_{SD} = index for surface damage) according to J. Deleume works [47]:

$$I_{SD} = \frac{Weakened\ length}{Gauge\ Length} \times 100 \text{ (Eq. 1)}$$

In Equation 1, the weakened length is calculated by considering the zones corresponding to a brittle fracture on the fracture surface. Their length is measured along the gauge length: the weakened length corresponds to the sum of the measured length values. Fig.4b shows an increase in I_{SD} values with the exposure duration for both metallurgical states, with, as expected, higher I_{SD} values for the T4 state compared to 150/20 samples. This suggested an increase in the area embrittled during the SCC exposure in relation to the increase in the corroded sites on the alloy surface. Moreover, the decrease in the elongation to failure itself, and the brittle fracture modes observed below the surface exposed to the NaCl solution were characteristic of the embrittlement induced by hydrogen in Al-Zn-Mg alloys. To go further in the understanding of the damage observed, two phenomena were distinctly studied: the anodic dissolution during the corrosion processes, and the contribution of hydrogen to the cracking process, which will be discussed in the next paragraphs.

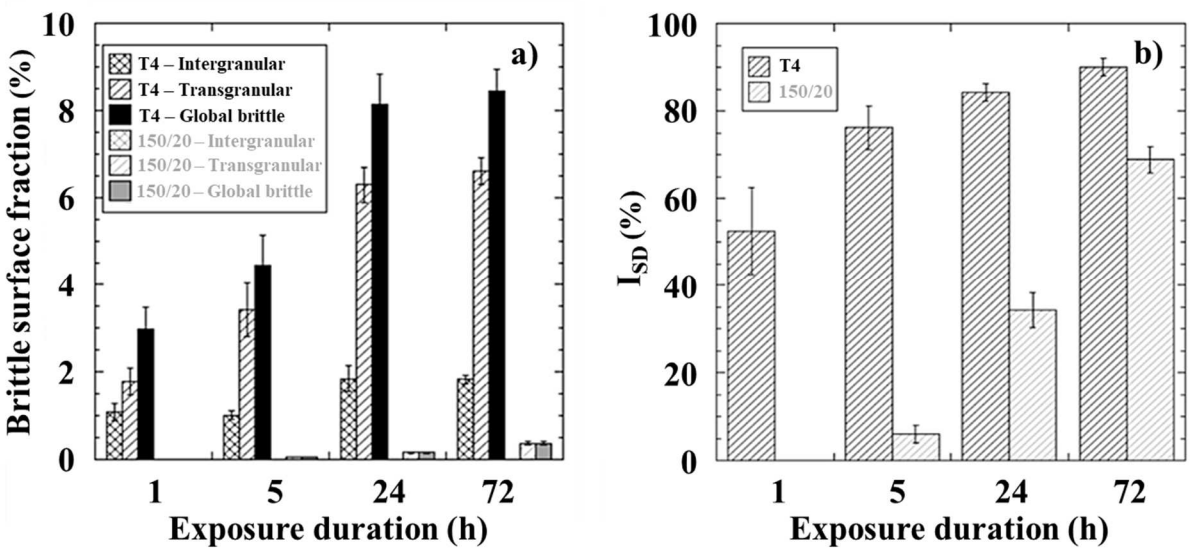

Fig. 4. Evolution of a) the brittle fracture areas on the fracture surfaces and (b) the I_{SD} values as a function of the exposure duration to the NaCl solution during SCC tests for the AA7046 – T4 and 150/20 samples.

b. About the influence of anodic dissolution on the mechanical properties of AA7046

Among the different theories as to why SCC occurs, the preferential corrosion along the GB (anodic dissolution) and the absorbtion of atomic hydrogen weakening the GB (hydrogen induced cracking) are generally cited. While evidence for the anodic dissolution is provided for 2xxx series, hydrogen-induced cracking is the favored mechanism for low Cu-7xxx series. As the exact mechanism remains controversial, the role of the anodic dissolution is examined in this part. In a first approach, the corrosion behaviour of the AA7046 was studied for the both metallurgical states. OCP measurements in 0.6 M NaCl solution with no stress applied showed that E_{corr} remained constant after 15 minutes of exposure and stabilized at approximately -0.94 V/SCE for the T4 state and -0.91 V/SCE for the 150/20 state (results not shown). The experiments were repeated 10 times, and led to the same gap between both metallurgical states. This difference was low, but, considering the repeatability of the results, it was assumed to be significant; it could be attributed to the η-$MgZn_2$ precipitates formed in the 150/20 state that reduced the Zn and Mg amounts in solid solution, leading to a global

ennoblement of the electrochemical potential [48,49]. Similar measurements carried out during the SCC tests showed no difference, suggesting that the stress applied had no significant effect on the electrochemical behavior of the alloy.

The micrographs in Figs. 5a and b show a comparison of the corrosion defects formed for both metallurgical states after 72 hours of exposure in 0.6 M NaCl solution, with no stress applied. Dissolution of the matrix was observed around all coarse precipitates observed due to galvanic coupling, for both T4 and 150/20 samples. Birbilis *et al*. [48] studied the local corrosion behavior of different intermetallic phases in 0.6 M NaCl solution and showed that $E_{corr}(Al_3Fe)$ and $E_{corr}(Al_3Ti)$ were higher than E_{corr}(7xxx matrix), which was consistent with these observations. After 24 hours of exposure, it was noticed that some dissolution areas turned into pits for the T4 state (Fig. 5a), even if cross-section observations revealed that they were not deeper than a few microns. No pit was observed for the 150/20 state surface even after 168 hours of exposure. As previously explained, the formation of η-$MgZn_2$ induced an ennoblement of the matrix for the 150/20 samples, which reduced the potential difference between the matrix and coarse precipitates. As a consequence, the galvanic coupling controlling the pits formation was delayed. In parallel, accelerated intergranular tests were carried out following the ISO 11846B standard. Samples were immersed for 24 hours in a corrosive solution ((30.0 ± 0.1 g) of NaCl + (10.0 ± 0.1 mL) of HCl 37%vol. in 1L of water) at 30°C. For both metallurgical states, no intergranular defect was observed. This was expected because of the low copper content of the alloy, reducing the risk of building any Cu-depleted zone around grain boundaries, which could have led to a potential gap between intergranular precipitates and the matrix [50].

Figs. 5c and 5d show cross-sections of the corrosion defects formed for the T4 and the 150/20 AA7046 samples, respectively, after 72 hours of SCC pre-exposure. It was observed that pits and dissolution phenomena were localized on the very near surface and could not

explain the loss of mechanical properties measured after tensile tests. However, after tensile tests at 10^{-3} s^{-1}, cracks were observed at the sample surface. Fig. 5e highlights a crack formed in a T4 sample. Electrochemical etching was carried out in order to characterize the crack paths; for the T4 samples, the observations showed that cracks were mainly intergranular (Fig. 5f). This was consistent with previous observations of brittle intergranular areas on the fracture surfaces of the T4 microstructure. In the 150/20 state, no crack propagation was observed, which was consistent with the fact that only shallow brittle transgranular fracture was observed. Cracks were also observed on the gauge length surface of the AA7046 tensile samples for both T4 and 150/20 metallurgical states (Figs. 5g and 5h); their length increased with the exposure duration to the NaCl solution. For both metallurgical states, the cracks were related to corrosion defects, and they were significantly longer for the T4 state, which was consistent with the higher loss of elongation to failure measured for this metallurgical state. In a first approach, this could be related to the higher corrosion kinetics measured for the T4 state. Indeed, potentiokinetic polarization curves were plotted for both the T4 and 150/20 samples in 0.6 M NaCl after a 15-min (72-h) holding step at OCP (results not shown). They showed a well-marked plateau in the cathodic domain attributed to the diffusion-controlled oxygen reduction; the anodic domain was characterized by an anodic peak followed by a passivity plateau. Therefore, the corrosion kinetics was controlled by the diffusion-controlled cathodic reaction, so that the corrosion current density i_{corr} was equal to the diffusion limit current. It was about 10^{-5} A cm^{-2} (10^{-6} A cm^{-2}) and 3 10^{-6} A cm^{-2} (5 10^{-7} A cm^{-2}) for the T4 and 150/20 samples, respectively for E=f(I) curves plotted after a 15-min (72-min) holding step at the OCP. However, as previously discussed, no corrosion defect deeper than a few microns beneath the alloy surface was observed regardless of the metallurgical state. As a consequence, the results suggested that the embrittlement was related to another phenomenon,

leading to study the hydrogen influence on the mechanical behaviour in the second part of this work.

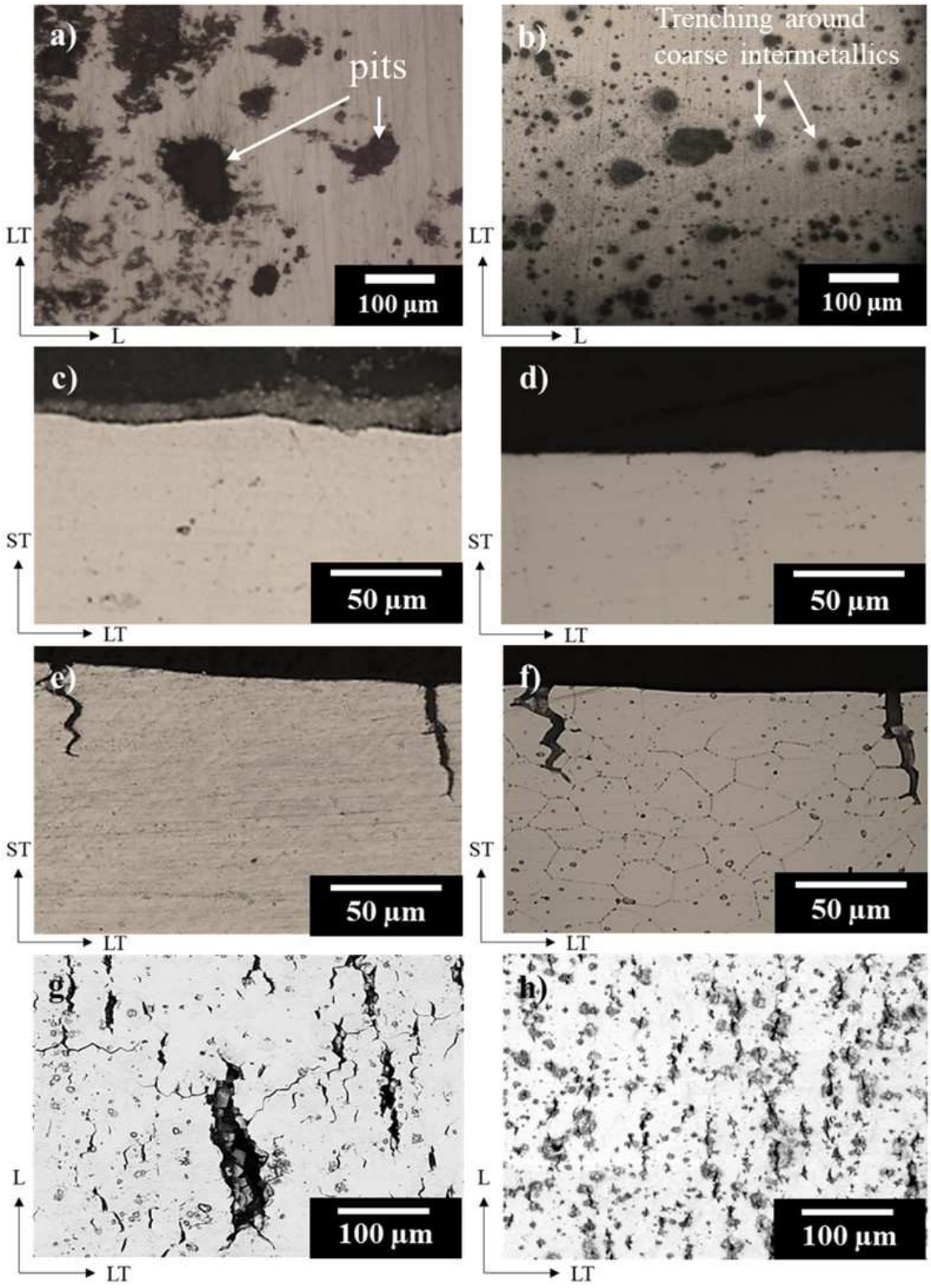

Fig. 5. OM micrographs of the surface of the AA7046 in the T4 (a) and 150/20 (b) state after 72 hours of exposure in 0.6 M NaCl solution. OM micrographs of cross-sections of the AA7046 – T4 (c) and 150/20 (d) after 72 hours in 0.6 M NaCl with a stress applied of 80 $\%YS_{0.2}$. e) and f) micrographs

show cracks in AA7046 – T4 after a SCC test for 72 hours followed by a tensile test in air at 10^{-3} s^{-1} before and after electrochemical etching in HBF_4, respectively. g) and h) are SEM micrographs of the surface of the gauge length of the 7046-T4 and 150/20 samples, respectively after a SCC test of 5 hours followed by a tensile test at 10^{-3} s^{-1} in air. Figs. a and b adapted from Fig. 1 in [34].

c. About the influence of the hydrogen on the mechanical behavior of AA7046

At first, a « Stress Corrosion Cracking susceptibility factor », I_{SCC}, was defined in order to compare the loss of elongation to fracture in both metallurgical states (Eq. 2). This was based on the difference of elongation to fracture between a non-exposed and a pre-exposed sample. Furthermore, it was necessary to take into account the scattering of the results for non-exposed samples to determine the relevancy of the I_{SCC} values. This was taken into account through $I_{baseline}$ (Eq. 3).

$$I_{SCC} = \frac{E_{f\ non-exposed\ sample} - E_{f\ corroded\ sample}}{E_{f\ non-exposed\ sample}} \times 100 \text{ (Eq. 2)}$$

$$I_{Baseline} = \frac{E_{f\ max} - E_{f\ min}}{E_{f\ average}} \times 100 \text{ (Eq. 3)}$$

Fig. 6 highlights a nonlinear increase in I_{SCC} values with the SCC exposure duration for both microstructures. This specific evolution was shown to be related to the increase in the hydrogen amount in the alloy [5,34]. This was more obvious concerning the T4 state for which the I_{SCC} and the hydrogen amount evolutions were very similar. This suggested that the damage was related to the corrosion-induced hydrogen. Indeed, inside the pits, the reduction of protons produced by the hydrolysis of the cations, led to hydrogen ingress into the alloy [4,7,28]. This was consistent with the fact that all cracks observed were related to the pits formed around intermetallic precipitates. For the 150/20 state, 72 hours of exposure were necessary to observe a significant decrease in the elongation to fracture, and this was also shown to be related to an increase in the hydrogen amount. This evolution was also in good agreement with previous results. Indeed, it was previously shown that the corrosion kinetic in the 150/20 state was slower, which was attributed to metallurgical changes. As a consequence, the amount of hydrogen that could penetrate in the alloy, and thus the loss of

mechanical properties were lower in the 150/20 state than in the T4 state. It was worth reminding here that the samples were pre-exposed to 0.6 M NaCl solution under mechanical loading (load equal to $0.8YS_{0.2}$). We measured the hydrogen uptake for samples exposed to a 0.6 M NaCl solution without mechanical loading in a previous work [34]. Similar hydrogen amounts were determined, which was relevant with our previous comment, i.e. the absence of significant influence of mechanical loading on the electrochemical behavior of the 7046 aluminium alloy (section 3b). Furthermore, we also analyzed in another previous work [33] the loss in mechanical properties for a T4 sample after pre-exposure to 0.6 M NaCl without mechanical loading for 24 hours. The elongation to fracture for the pre-exposed sample was 15 %, while it was 18.3 % for the non-exposed sample, leading to an I_{SCC} value of 18 %. This I_{SCC} value was similar to that determined in the present work (Fig. 6 a), i.e. 19 %, for a sample pre-exposed for 24 hours with a $0.8YS_{0.2}$ stress applied. Finally, the detailed analysis of the fracture mode for the sample pre-exposed without mechanical loading [33] showed a fracture surface with brittle intergranular fracture zones (surface fraction of 1.5 %) and quasi-cleavage fracture zones (surface fraction of 5 %), which was similar to the fracture surface observed in the present work for the sample pre-exposed under mechanical loading: about 1.75 % of the fracture surface corresponding to brittle intergranular fracture mode and 6.25 % to transgranular fracture mode. The comparison of the results obtained in the present study with those of our previous works [33,34] suggested, for the experimental conditions tested, that there was no significant influence of the stress on hydrogen adsorption.

Concerning the differences in hydrogen content between the two metallurgical states (Fig. 6), other hydrogen – microstructural features interactions could also explain those differences. In our previous study concerning the AA7046 [25], measurements of the hydrogen penetration depth by SKPFM showed that hydrogen diffusion was slowed down in the 150/20 state compared to the T4 state. It was proposed that the formation of intragranular

η-$MgZn_2$ precipitates in the 150/20 samples limited the damage, which was attributed to hydrogen trapping around the intragranular η-$MgZn_2$ precipitates which would limit its diffusion. In parallel, hydrogen accumulation in the subsurface due to trapping led to a lower gradient in hydrogen amount between the alloy and the surface exposed to the corrosive environment. This could lead to a slower hydrogen penetration, and thus to lower hydrogen content in the 150/20 samples. This could also explain the limited loss of mechanical properties of the pre-exposed 150/20 state, a critical hydrogen amount being probably required to lead to a significant embrittlement.

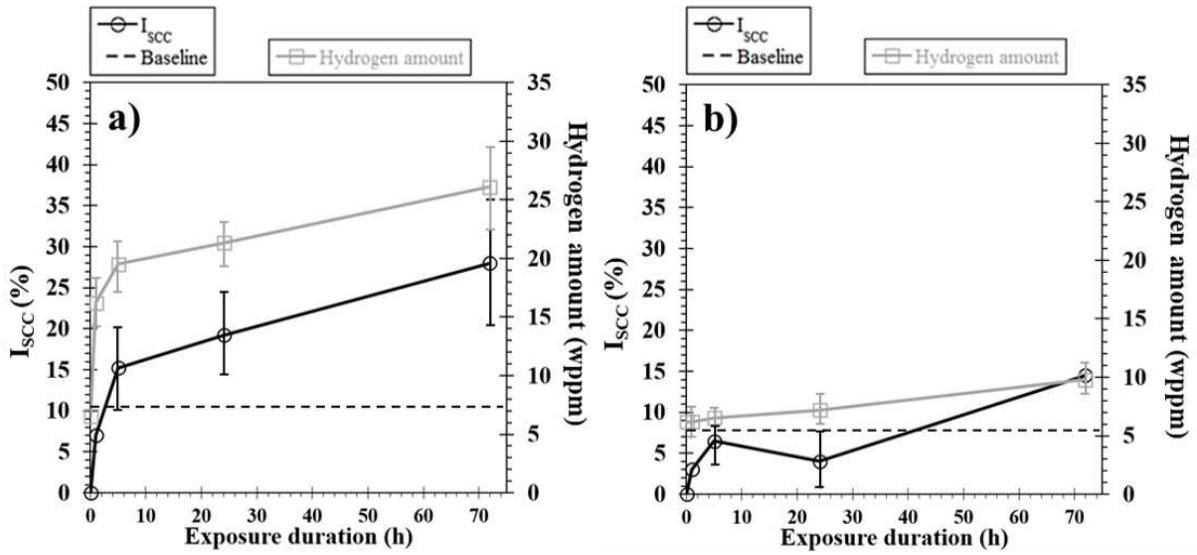

Fig. 6. Comparison of the evolution of I_{SCC} and of the hydrogen amount with the exposure duration in 0.6 M NaCl with a stress applied of 80 %$YS_{0.2}$ for the AA7046 – T4 (a) and 150/20 (b).

4. Discussion

a. Hydrogen charging during corrosion processes

The new results obtained by comparing the evolution of mechanical properties for the AA7046 pre-exposed under SCC tests to experimental measurements of the hydrogen global amounts led to propose a global mechanism discussed below regarding the results of previous works and of recent studies. According to the previous results, it was shown that AA7046 was

not susceptible to SCC due to intergranular dissolution, but almost exclusively to hydrogen diffusion and hydrogen-induced cracking, a phenomenon largely supported [5,7,37,51,52]. Fig. 7 shows first that hydrogen was produced during SCC exposure according to the following global reaction [7]:

$$Al^{3+} + 3H_2O \rightarrow Al(OH)_3 + 3H^+ \text{ (Eq. 4)}$$

This was confirmed by the presence of cracks after tensile tests in air exclusively localized around pits developed during SCC pre-exposure. Even if the influence of the stress applied during the SCC pre-exposure was not clearly demonstrated in this study, Wang *et al.* [53] showed that the stress-corrosion coupling was decisive for hydrogen penetration in aluminium alloys from the 2xxx and 7xxx series, when they were immersed in an aqueous solution. They supposed a hydrogen – crack tip interaction, especially supported by authors like Najjar *et al.* [7]: the tip would be the penetration area due to the high stress triaxiality ratio. However, in the specific case of the AA7046, no crack formation was highlighted during SCC pre-exposure, even after 72 hours, whereas a significant increase in the hydrogen amount was measured with time exposure. This suggested that for the AA7046, the stress-corrosion coupling was not of major importance. The stress probably acted by breaking the native passive layer already stressed during corrosion [54], favouring corrosion reactions. Altenbach et al. [52] studied the phenomenon by synchrotron-based holotomography and X-ray fluorescence. They associated the hydrogen penetration to a cathodic reaction which led to high hydrogen partial pressure allowing hydrogen absorption and then diffusion in the alloy. In their work, Schwarzenböck *et al.* [10] suggested that the formation of topographic steps near the grain boundaries and especially the softer PFZ, could lead to the rupture of the passive layer and thus promote the hydrogen absorption at the grain boundaries and its segregation.. In the same way, in a previous study about slow strain rate tensile tests [34], we showed that the hydrogen penetration could be enhanced by the sub-surface deformations and

the local accumulation of dislocations. A reciprocal effect was discussed between hydrogen intake from the laboratory air and dislocations accumulation at the alloy surface.

The formation of η intragranular precipitates in the 150/20 state led to a global ennoblement of the matrix that reduced the potential difference between coarse intermetallic precipitates and the matrix [48]. As a consequence, the driving force for galvanic coupling reduced and the pitting formation kinetic was slowed down. This led to the decrease in the hydrogen ingress.

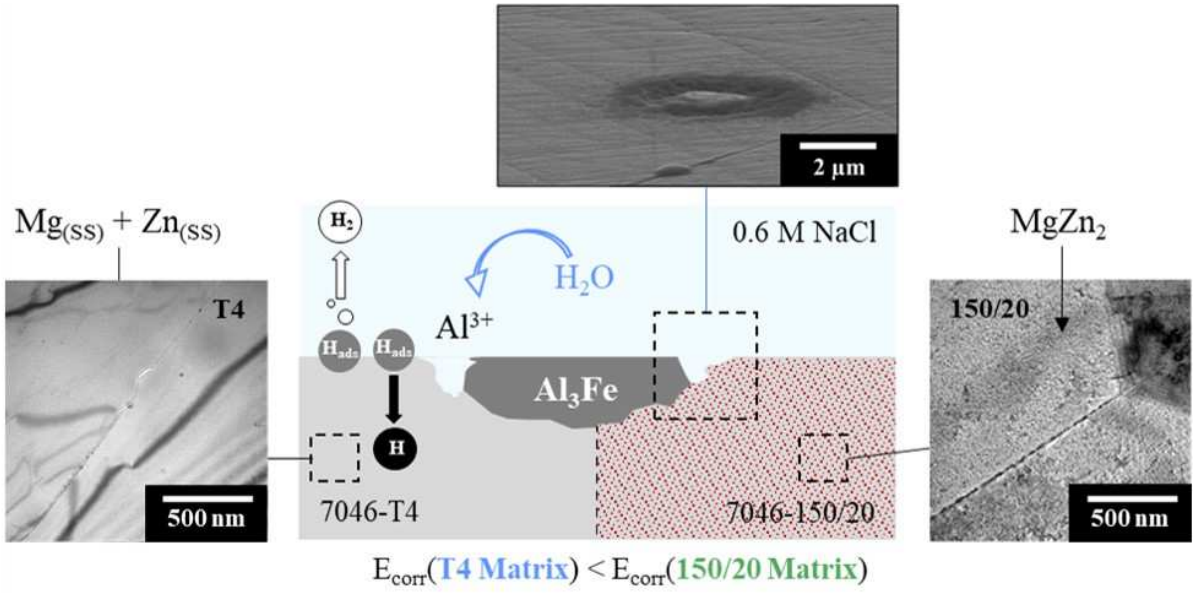

Fig. 7. Schematic representation of the hydrogen cathodic charging during SCC exposure: the matrix dissolution around (also shown on SEM micrograph) the coarse intermetallic precipitates led to hydrogen absorption in both metallurgical states. TEM micrographs of the T4 and 150/20 states show the differences of microstructures.

b. Hydrogen diffusion and trapping

Previous works led to the conclusion that the decrease in the elongation to fracture was larger in the microstructures where brittle intergranular fracture was observed [25]. This was supported by several authors [7,10,52,55]**.** The idea of hydrogen diffusion and localization enhanced at the grain boundaries was specifically discussed by Song *et al.* [55] for 7xxx aluminium alloys. They reported an affinity between absorbed hydrogen and Mg micro-

segregations at the grains boundaries compared to other elements like Al, which would thus increase the hydrogen diffusion rate. Recent work based on Density Functional Theory (DFT) calculations showed the H-Mg affinity, but the authors also discussed the fact that the nature of isolated impurities like Zn and Mg was not a first order parameter to explain the hydrogen accumulation compared to structural defects [56]. Moreover, the authors found that another parameter involved was the local stress, either in tension or in compression, with which the hydrogen has a stronger affinity. Concerning the 150/20 state, hydrogen trapping on intragranular η-$MgZn_2$ precipitates seemed to only lead to transgranular fracture which could be explained either by the fact that the hydrogen could not penetrate deep enough in the alloy, or by the fact that intergranular diffusion was limited by the coarsening of η-$MgZn_2$ intergranular precipitates. This was also confirmed after SCC exposures and supported by hydrogen induced cracking theories proposing that the hydrogen could be easily trapped at stable phases interfaces, limiting thus the hydrogen diffusion [52]. In our previous work [25], we especially showed that the increase in the (Mg,Zn)-rich precipitates size thanks to heat treatments increased their trapping efficiency. The coherent and semi-coherent precipitates were shown to have less affinity with the hydrogen than the incoherent η-$MgZn_2$ stable precipitates. It could be noted here that in other aluminium alloy systems (e.g. 2024 aluminium alloy), hydrogen could be trapped by the stress fields of coherent GP zones and precipitates [57].

These hypotheses being based on the intergranular diffusion of the hydrogen without experimental assertions, complementary experiments were carried out in the present work to discuss this phenomenon. T4b microstructures characterized by a higher grain size were obtained by heat treatments as described in the experimental part. A heterogeneous increase in the grain size was observed after 48 hours of heat treatment, with grains varying from 30 µm to several mm. However, for the purpose of this study, it was considered that the decrease in

the surface fraction of grain boundaries was sufficient. After the heat treatment, Vickers hardness measurements were carried out during several weeks; results showed a stabilization after two weeks at 127 ± 3 HV_{500g} compared to 152 ± 2 HV_{500g} in the T4 state. This was consistent with the grain coarsening according to the Hall-Petch relationship. Samples of AA7046 in the T4 and T4b states were then hydrogen cathodically charged in H_2SO_4 for 72 hours. The aim was to compare the estimated hydrogen penetration depth in both microstructures to evaluate the hydrogen diffusion coefficient along the grain boundaries thanks to SKPFM measurements. Results concerning the T4 sample after hydrogen pre-charging as well as without pre-charging are reported from our previous work [25].

Fig. 8a shows the evolution of the surface potential of the T4 reference sample neither exposed to SCC tests nor hydrogen charged in sulfuric acid. It can be noticed that the potential value remains stable except for local variations related to the tip passing over coarse intermetallic precipitates. An average value of 1.45 V was measured for this run, but as discussed in our previous works [25], this value depended on the environmental parameters like relative humidity. As a consequence, and in order to make all runs comparable, a ΔV value corresponding to the difference between the potential measured in the hydrogenated volume of the samples and the potential measured in the core of the specimens was considered. Fig. 8b shows the evolution of ΔV for both the T4 and the T4b state after hydrogen pre-charging in sulfuric acid. A potential gradient was measured and indirectly related to hydrogen concentration as discussed in our previous work [25]. For the T4 samples, a repeatable hydrogen penetration depth of 275 ± 15 μm was obtained, whereas for T4b samples, the measured depth was significantly lower, i.e. 110 ± 60 μm. The lower hydrogen penetration depth in the T4b state suggested a predominance of the intergranular diffusion in the AA7046.

By comparison of the measured hydrogen penetration depth to the Fick's 2nd law equation (Eq. 5), it was possible to estimate the effective hydrogen diffusion coefficients of 1.5-8.10^{-15} $m^2.s^{-1}$ in the T4b state, and of 2.2.10^{-14} $m^2.s^{-1}$ in the T4 state. In Eq. 5, *c(x)* is the hydrogen concentration at a distance *x* from de charged surface, c_0 is the initial concentration in the bulk of the alloy (considered equal to 0 for t = 0 and x > 0), c_S is the hydrogen concentration at the alloy surface during charging (= 1 for t > 0 and x = 0) and *t* is the charging time.

$$\frac{c(x)-c_s}{c_0-c_s} = erf\left(\frac{x}{2\sqrt{D_{app}t}}\right) \text{ (Eq. 5)}$$

The dispersion measured in the SKPFM measurements for the T4b state could be explained by the heterogeneity in the grain size. Moreover, such a dispersion could be also explained by different thicknesses of the oxides formed on different grains, due to their respective orientation. In the T4 state, this effect was balanced by the higher number of grains. It can also be related to the grain anisotropy in the thickness of the sample in the T4b microstructure.

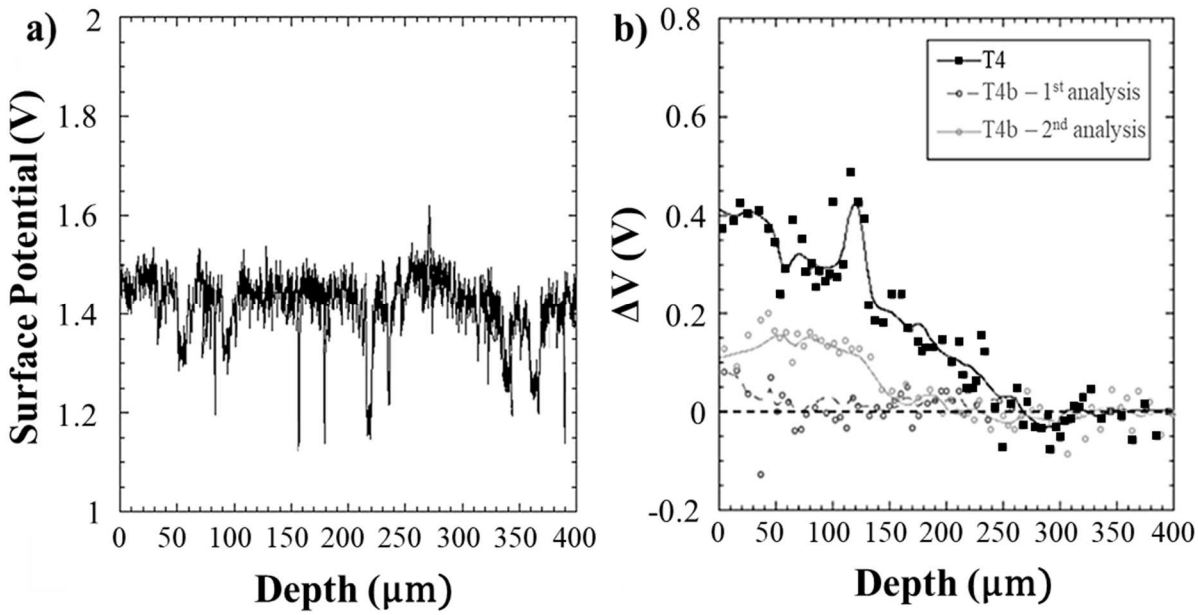

Fig. 8. a) Evolution of the Volta potential in the AA7046 – T4 without hydrogen. b) Comparison of the evolution of the ΔV gradient in the AA7046 – T4 and in the T4b states after 72 hours of charging in H_2SO_4 pH 2 with an applied potential of -1.450 V/SCE. Fig. a) and the curve plotted for T4 sample in b) have been adapted from [25].

A comparison between the global hydrogen diffusion in the T4 and T4b microstructures was proposed, using the Hart's relationship as a first approach [58]:

$$D_{eff} = g{D_H}^{GB} + (1-g){D_H}^{G} \text{ (Eq. 6)}$$

where D_{eff} is the effective hydrogen diffusion coefficient in the alloy, ${D_H}^{GB}$ and ${D_H}^{G}$ are the effective hydrogen diffusion coefficients at the grain boundaries and in the grains, respectively. δ is the average width of the grain boundaries (approximately 1 nm), d is the average diameter of the grains (30 µm in the T4 and 2 mm in the T4b), and $g = \delta / d$. The effective hydrogen diffusion coefficient can be described for both microstructures as follows:

$${D_{H,app}}^{T4} = g_{T4}{D_H}^{GB} + (1-g_{T4}){D_H}^{G} \text{ (Eq. 7)}$$

$${D_{H,app}}^{T4b} = g_{T4b}{D_H}^{GB} + (1-g_{T4b}){D_H}^{G} \text{ (Eq. 8)}$$

The values of ${D_{H,app}}^{T4}$ and ${D_{H,app}}^{T4b}$ estimated thanks to SKPFM measurements allow the effective diffusion in the grains and at the grain boundaries to be determined:

$${D_H}^{G} = \frac{1}{d_{T4}-d_{T4b}}\left(d_{T4}{D_{H,app}}^{T4} - d_{T4b}{D_{H,app}}^{T4b}\right) \text{ (Eq. 9)}$$

$${D_H}^{GB} = \frac{1}{g_{T4b}}\left({D_{H,app}}^{T4b} - (1-g_{T4b}){D_H}^{G}\right) \text{ (Eq. 10)}$$

With this approach, diffusion coefficients of 1.5 – 8.10^{-15} $m^2.s^{-1}$ and of 2.1 – $3.1.10^{-10}$ $m^2.s^{-1}$ were calculated in the grains and at the grain boundaries, respectively. This could be summarized as a difference of approximately 5 orders of magnitude between the intergranular and the grain diffusion coefficients. The predominance of the intergranular diffusion was thus demonstrated, confirming the role of these short-circuit diffusion paths in the mechanisms of SCC in the AA7046. Ichimura *et al*. showed that the grain boundaries in aluminium have complex effects on hydrogen diffusivity [59]. They talked about 'the grain boundary cross effect' which refers to an enhanced diffusion along a straightforward grain boundary and a

suppressed diffusion at grain boundary nodes by trapping of hydrogen. More recently, Pedersen *et al.* proposed an alternative explanation for Ichimura's results [60]. Nevertheless, they also evidenced the complex effect of the grain boundaries on hydrogen diffusion. Such a complex effect can be explained by considering that many parameters have to be taken into account, e.g. the hydrogen concentration [61, work about palladium], as well as the structure and chemistry of the grain boundaries as indicated by Chene *et al.* [62]. For example, Saitoh *et al.* [63] showed that the precipitate-free grain boundaries were capable of short circuit path. Therefore, it is clearly seen from these different studies that the lattice diffusivity and grain boundaries diffusivity values can be significantly different in some cases. Those studies also showed that it is difficult to give definitive values for the lattice and grain boundaries hydrogen diffusivities. In their study, Ichimura *et al.* gave a comparative survey for the hydrogen diffusivity data and showed that the diffusion coefficients did not agree well with each other [59], which can be explained by referring to the previous discussion. Young and Scully also mentioned a large scatter in reported values of the diffusivity of hydrogen in aluminium [19]. Nevertheless, it could be noted that Chene *et al.* estimated the hydrogen diffusion in impure aluminium, and proposed a values of 2.3 10^{-14} cm^2 s^{-1} from an extrapolation of high temperature [62]. This value was similar to the lattice diffusivity value we found in the present study.

Consequently, in the T4 state, the hydrogen produced during corrosion processes could diffuse in the alloy across the grain boundaries leading to both:

- a preferential localization of the hydrogen at the grain boundaries;
- a higher hydrogen penetration depth.

Finally, the different steps of the hydrogen embrittlement corresponding to diffusion and trapping were schematically represented in Fig. 9. Concerning the T4 state, once produced during corrosion processes, the hydrogen could diffuse in the matrix where it did not "meet"

any trapping site. In this metallurgical state, the main traps were dislocations, grain boundaries and intergranular precipitates. Bhuiyan *et al.* [64] observed by microtomography an increased rate of trapping site occupancy at grain boundaries compared to other trapping sites like dislocations or vacancies. In Fig. 9b, two areas numbered (1) and (2) were defined as respectively high and low hydrogen concentration zones. In the hydrogenated deep area (zone 2), the hydrogen should be mainly located at the grain boundaries thanks to the high diffusivity of the hydrogen at the grain boundaries as demonstrated. Only the few $MgZn_2$ intergranular precipitates could act as limiting trapping sites for the hydrogen diffusion. However, it could be argued that, when these trapping sites are saturated with hydrogen, the hydrogen could then keep diffusing at the grain boundaries. Furthermore, the number of intergranular precipitates in the T4 state were probably too low to efficiently limit the hydrogen diffusion. Therefore, the grain boundaries should act as short-circuit diffusion paths as suggested by several authors [7,25,37,52,55], and as demonstrated above with SKPFM measurements.

On the contrary, in the 150/20 state, Figs. 9c and 9d propose that the hydrogen was trapped near intragranular η-$MgZn_2$ precipitates (2) and intergranular coarse precipitates (1) leading to a limitation of the global diffusion of the hydrogen. We showed in a previous work that in the AA7046, the hydrogen apparent diffusion coefficient decreased due to the formation of the intragranular η-$MgZn_2$ precipitates [25]. More specifically, it was assumed that the trapping occurred at the precipitates/matrix interface. This was confirmed by the fact that the hydrogen penetration depth decreased with the coherency of these precipitates. Several works confirmed these assertions [5,65–67]. Scamans *et al.* [5] suggested that only η precipitates bigger than 25 nm corresponding to a crystal size were able to act as irreversible trapping sites for hydrogen. Two consequences could be drawn:

- the limited hydrogen diffusion led to the localization of the hydrogen in the vicinity of the coarse precipitates surrounded by dissolved matrix. As a consequence, the driving force for hydrogen penetration was reduced, explaining the lower hydrogen global amounts measured in Fig. 6 for the 150/20 state compared to the T4 state. In the T4 state, when absorbed, the hydrogen could easily diffuse in the bulk alloy, avoiding its surface accumulation. The hydrogen absorption was thus less limited.
- for 150/20 samples, the hydrogen diffusion was limited in the bulk and along the grain boundaries by the intragranular η-$MgZn_2$ precipitates, which was consistent with the shallow brittle areas observed on the fracture surfaces in Fig. 3f.

In both microstructures, the hydrogen was also shown to have affinity with dislocations which was taken into account in Fig. 9b and 9c. This will be of major importance to explain the final fracture as will be discussed further down in the article [68].

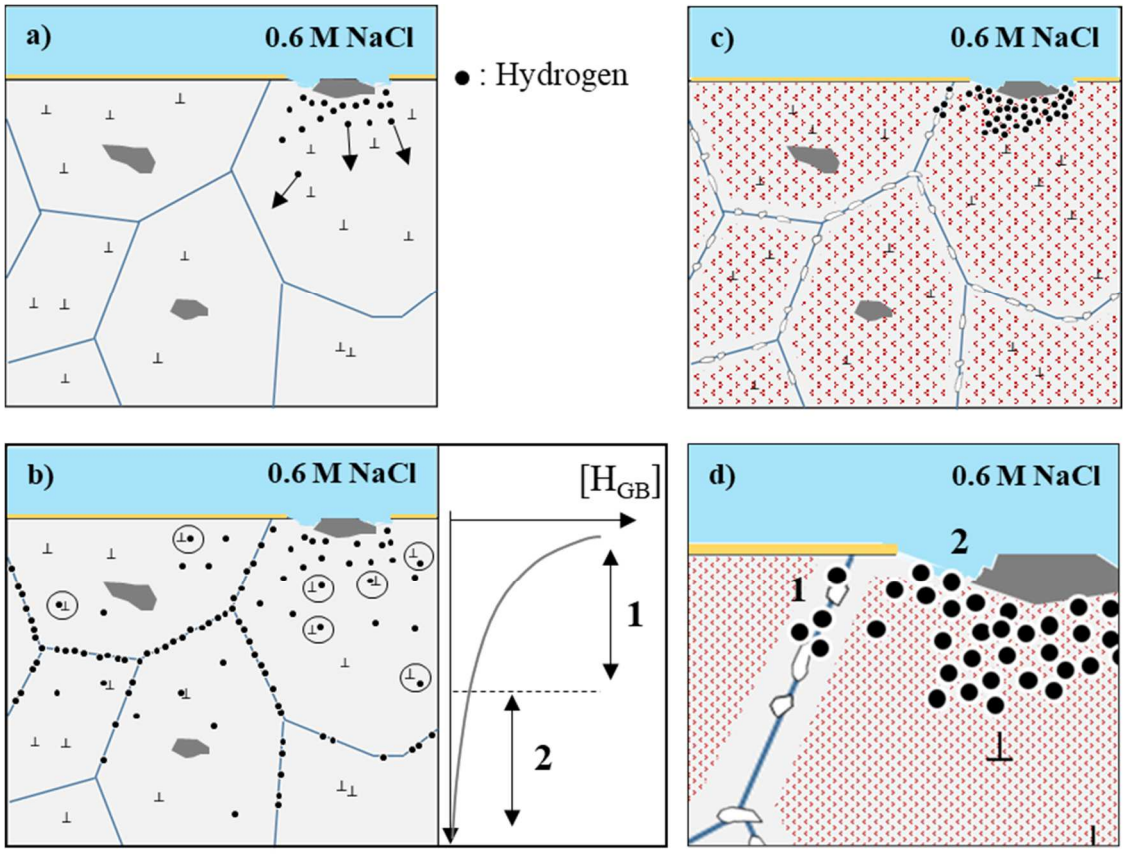

Fig. 9. Hydrogen diffusion and distribution in the AA7046 – T4 (a and b) and 150/20 (c and d). Figures a and c schematically represent the first step of the hydrogen diffusion in the alloy in the direct

vicinity of the coarse precipitates surrounded by dissolved matrix. The (⊥) represents the dislocations and the red dots corresponds to the intragranular η-$MgZn_2$ precipitates. Figures b and d represent the following steps. On figure b, a representation of the hydrogen concentration at the grain boundaries is given.

c. Hydrogen transport and fracture

Finally, the last step of the SCC mechanism corresponding to the transport of hydrogen and the final fracture was discussed. Fig. 10 describes the cracking sequence in the AA7046 – T4. Under the surface, corresponding to the area numbered (1) of Fig. 9, the hydrogen concentration at the grain boundaries was high enough to allow a decrease in the intergranular cohesion stresses (Fig. 10a). Due to the progressive strain applied, dislocations were formed and as discussed in previous work [34], the interstitial hydrogen could be trapped by these dislocations due to the resulting elastic distortion [63,69]. Saitoh *et al.* [63] showed by tritium autoradiography the preferential location of hydrogen in the dislocation network. This trapped hydrogen could then be drained by dislocations and could be redistributed as demonstrated in our previous work with samples tested by slow strain rates in ambient atmosphere [34]. Fig. 10b shows that the dislocations were preferably located near the grain boundaries when the strain increased, which explained the ductile-intergranular fracture for non-exposed samples. During this process, the hydrogen that was trapped on dislocations was therefore transported up to the grain boundaries and consequently, the intergranular hydrogen amount increased.

Finally, when the strain went on increasing, Fig. 10c shows that cracks could form as a result of a synergy between high dislocations density and high hydrogen concentrations at the grain boundaries. Moreover, several works suggested that the hydrogen could favour local plasticity by reducing inter-dislocations interactions and dislocations – microstructural parameters interactions. Robertson *et al.* [32,70] showed a decrease in the distance between dislocations in the presence of hydrogen in an austenitic 310S steel. Similar observations were made by TEM in aluminium alloys by Ferreira *et al.* [32]. This led to brittle intergranular

fracture (Fig. 10f). The cracks formed then propagated in the alloy up to the 2nd area ((2) in Fig. 9b) where the hydrogen amount was lower. In this zone, the hydrogen concentration at the grain boundaries was not sufficient to allow intergranular decohesion and thus brittle intergranular fracture. However, during the crack propagation, the plasticity increased at the crack tip (Fig. 10d). In these plastic areas, the hydrogen promoted dislocations accumulation as previously discussed, but it also promoted the accumulation of dislocations in the same direction of the lattice. This effect was due to a decrease in the probability of deviated gliding of dislocations due to hydrogen as proposed by Ferreira *et al.* [70]. The main consequence was the decohesion of a specific plane in the fcc structure which led to transgranular decohesion (Fig. 10e) and the brittle transgranular fracture (Fig. 10g) observed in the T4 microstructure. In their recent work, Xie *et al.* [71] showed that the local plasticity related to the increase in dislocation density at the crack tips could favor the formation of substructures of low angle grain boundaries which could enhance intergranular cracks after hydrogen enrichment.

Concerning the 150/20 metallurgical state, a large amount of studies focused on the influence of the intergranular and intragranular precipitates composition and structure on the SCC resistance of Al-Zn-Mg alloys [43,72,73]. In the current study, it was proposed that the hydrogen was trapped in the grains around intragranular η-$MgZn_2$ precipitates and therefore could not diffuse along the grain boundaries. As a consequence, no brittle intergranular fracture could be observed after tensile tests at 10^{-3} s^{-1}. On the contrary, mainly brittle transgranular fracture was observed due to the weakening of interatomic bonds leading to interfacial decohesion. This was suggested by SKPFM work [25] and confirmed by recent works of Safyari *et al.* [68]. In the same way, Krishnannuni *et al.* [23] showed that, in the T73 conditions, a 7010 aluminium alloy showed no brittle intergranular fracture which was associated with the homogeneous distribution of η-$MgZn_2$ precipitates in the grains. On the

contrary, in the T6 conditions, where the intragranular precipitates were semi-coherent, intergranular fracture was observed. Wang *et al.* [74] confirmed that the coarsening of the grain boundary precipitates was beneficial for SCC resistance of Al-Zn-Mg alloys. The hydrogen trapping on coarse intergranular precipitates seems to reduce the crack nucleation along grain boundaries [55,75,76].

High concentrations of hydrogen in the grains promoted the nucleation of dislocations and as for the T4 state, the inhibition of the deviated gliding promoted the accumulation of dislocations in dense planes. This led to the brittle transgranular fracture. However, hydrogen could also favour intergranular decohesion in the 150/20 state when tested at slow strain rates as evidenced in the literature [34,77]. Indeed, the hydrogen transport by dislocations could induce hydrogen relocation at the grain boundaries. When a sufficient hydrogen concentration was reached, intergranular fracture could be observed. Recently, Safyari *et al.* [68] showed that, in cold-rolled Al-Zn-Mg alloys, large amounts of hydrogen trapped at dislocations led to hydrogen-induced intergranular fracture. They also showed that, in the presence of second phase particles, the distribution of the hydrogen between the precipitates and the dislocations improved the hydrogen embrittlement resistance of these alloys by decreasing the dislocation motion induced hydrogen mobility.

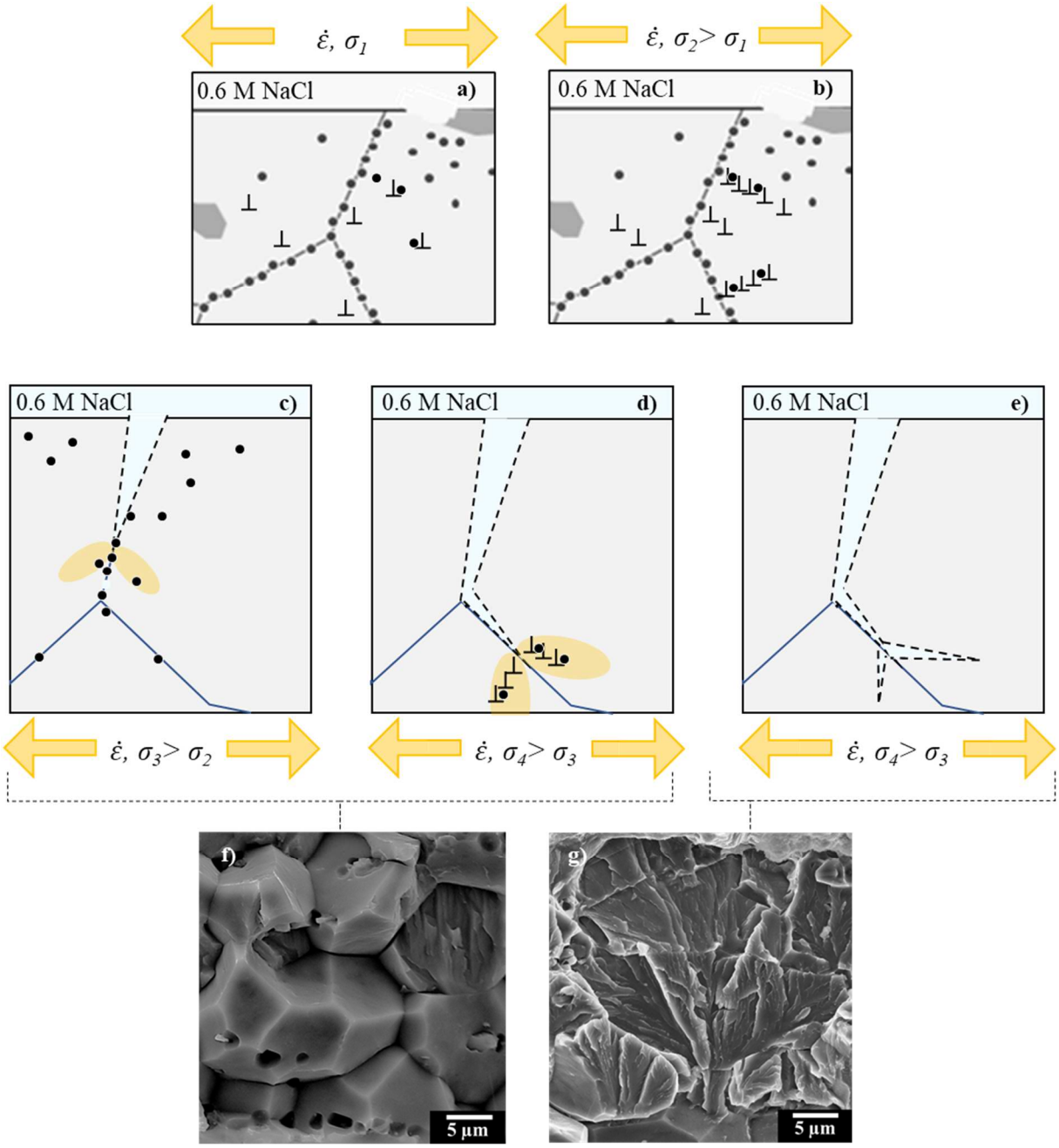

Fig. 10. Schematic representation of the fracture process after SCC pre-exposure in the AA7046 – T4. a) shows the first step of the deformation leading to the formation of dislocations and trapping of reticular hydrogen near dislocations. b) shows the formation of the dislocations network and the localization of dislocations near the grain boundaries leading to an increase in the local hydrogen concentration and of the plasticity. c) intergranular cracks form as a consequence of the high hydrogen concentration and plasticity. d) the intergranular crack propagation leads to an increase in the plasticity at crack tips finally leading to transgranular cracks (e). Brittle intergranular (SEM image f) and transgranular (SEM image g) fracture resulting from (c, d) and (e), respectively.

5. Conclusions

The role of the hydrogen during SCC processes in the AA7046 aluminium alloy was investigated for two metallurgical states and discussed regarding the results of previous

works. The aim of the present study was to improve the current understanding of SCC mechanisms in low-copper 7xxx aluminium alloys and bring experimental evidence for the influence of the hydrogen. The following conclusions were drawn:

1. The specificity of the AA7046, containing low copper amounts, was its relatively high resistance to intergranular and pitting corrosion. In agreement with the 'hydrogen embrittlement' favored SCC mechanism for low Cu-7xxx series, the anodic dissolution theorie was discarded, as no susceptibility to intergranular corrosion was observed. The surface of the alloy was only affected by trenching, i.e. local dissolution of the matrix around the coarse intermetallics, after a short exposure in the chloride media and by pits after longer exposures. It was shown that the 150/20 state was less susceptible to pitting corrosion than the T4 state, which was assumed to be related to the modification of the matrix composition following the formation of intragranular η-$MgZn_2$ precipitates.
2. After pre-exposure under stress in 0.6M NaCl, the elongation to fracture decreased for both metallurgical states although to a much lesser extent for the 150/20 state. A study of the corrosion defects propagation showed that the loss of mechanical properties could not be explained by the corrosion defects. However, an in-depth analysis of the fracture surface close to the surface exposed to the NaCl solution during SCC pre-exposure revealed brittle intergranular fracture and quasi-cleavage areas in the T4 state, whereas only shallow quasi-cleavage areas for the 150/20 state are observed. These changes of the fracture modes were assumed to be related to hydrogen produced during corrosion exposure. In the present work, pre-exposure was done under sustained load ($0.8YS_{0.2}$), but comparison with previous works performed with pre-exposure without load showed no significant influence of the stress on the hydrogen uptake, for the experimental conditions tested.

3. Global hydrogen measurements in the alloy after different durations of SCC pre-exposure revealed a direct relationship between the loss in elongation to fracture and the hydrogen amount. A long exposure was required in the 150/20 state to produce a significant hydrogen amount, contrary to the T4 state for which a few hours are enough. This was explained by the lower susceptibility to pitting corrosion of the 150/20 state compared to the T4 sample. It was also explained by hydrogen diffusion at the grain boundaries for the T4 sample, while hydrogen was trapped at the intragranular η-$MgZn_2$ for the 150/20 sample, as summarized in points 4 and 5.
4. The role of grain boundaries as short-circuit diffusion paths was demonstrated based on the comparison of the T4 and T4b states. For the AA7046-T4, the model postulates that the accumulation of dislocations at grains boundaries allowed high local hydrogen concentration and the decrease in the intergranular cohesion stresses, leading to brittle intergranular fracture. The crack propagation leading to local increased plasticity at the crack tips ultimately led to brittle transgranular fracture.
5. In the 150/20 state, the model favors a role of the intragranular η-$MgZn_2$ precipitates as hydrogen traps which agreed for the lower hydrogen effect on the mechanical properties for this microstructure. The accumulation of dislocations in a single direction in the lattice favored by hydrogen led to transgranular decohesion and to brittle but shallow transgranular surface cracks.

Credit authorship contribution statement

L. Oger: Investigations. Formal analysis. Visualization. Methodology. Data curation. Writing-original draft. Writing-Review&Editing. **E. Andrieu**: Methodology. Conceptualization. Formal analysis. Writing-Review&Editing. **G. Odemer**: Methodology. Formal analysis. Writing-Review&Editing. **L. Peguet**: Supervision. Validation. Conceptualization. Project administration. Resources. Writing-Review&Editing. **C. Blanc**:

Funding acquisition. Methodology. Project administration. Supervision. Validation. Conceptualization. Formal analysis. Data curation. Writing-Review&Editing.

Aknowledgements

The authors thank the ANRT for their financial support (L. Oger PhD thesis). They thank Constellium Technology Center (Voreppe, France) for its financial support and for providing the materials. They also thank Cedric Charvillat and Manon-Chloé Lafouresse for their help with the SKPFM and Ronan Mainguy for his help for SCC and mechanical tests.

References

[1] Aluminium in cars, in: EAA Broch., 2012.

[2] J. Hirsch, Recent development in aluminium for automotive applications, Trans. Nonferrous Met. Soc. China. 24 (2014) 1995–2002. https://doi.org/10.1016/S1003-6326(14)63305-7.

[3] T. Mao, T. Altan, Aluminum sheet forming for automotive applications, Part I, Stamp. J. (2013).

[4] N.J.H. Holroyd, G.M. Scamans, Stress corrosion cracking in Al-Zn-Mg-Cu aluminum alloys in saline environments, Metall. Mater. Trans. A Phys. Metall. Mater. Sci. 44 (2013) 1230–1253. https://doi.org/10.1007/s11661-012-1528-3.

[5] G.M. Scamans, R. Alani, P.R. Swann, Pre-exposure embrittlement and stress corrosion failure in AlZnMg Alloys, Corros. Sci. 16 (1976) 443–459. https://doi.org/10.1016/0010-938X(76)90065-2.

[6] L. Christodoulou, H. Flower, Hydrogen embrittlement and trapping in Al6%-Zn-3%-Mg, Acta Metall. 28 (1980) 481–487. https://doi.org/10.1016/0001-6160(80)90138-8.

[7] D. Najjar, T. Magnin, T. Warner, Influence of critical surface defects and localized competition between anodic dissolution and hydrogen effects during stress corrosion cracking of a 7050 aluminium alloy, Mater. Sci. Eng. A. 238 (1997) 293–302. https://doi.org/10.1016/S0921-5093(97)00369-9.

[8] K.R. Hebert, Trapping of Hydrogen Absorbed in Aluminum during Corrosion, Electrochim. Acta. 168 (2015) 199–205. https://doi.org/10.1016/j.electacta.2015.03.198.

[9] W. Gruhl, Zeitschrift fuer Metallkunde, Zeitschrift Fuer Met. 75 (1984) 819–826.

[10] E. Schwarzenböck, L. Wiehler, T. Heidenblut, T. Hack, C. Engel, H.J. Maier, Crack initiation of an industrial 7XXX aluminum alloy in humid air analyzed via slow strain rate testing and constant displacement testing, Mater. Sci. Eng. A. 804 (2021) 1–12. https://doi.org/10.1016/j.msea.2021.140776.

[11] J.R. Scully, G.A. Young Jr., S.W. Smith, Hydrogen Solubility, Diffusion and Trapping in High Purity Aluminum and Selected Al-Base Alloys, Mater. Sci. Forum. 331–337 (2000) 1583–1600. https://doi.org/10.4028/www.scientific.net/MSF.331-337.1583.

[12] N. Ben Ali, D. Tanguy, R. Estevez, Effects of microstructure on hydrogen-induced cracking in aluminum alloys, Scr. Mater. 65 (2011) 210–213. https://doi.org/10.1016/j.scriptamat.2011.04.008.

[13] X. Chen, S. Zhai, D. Gao, Y. Liu, J. Xu, Y. Liu, Enhanced stress corrosion cracking resistance and electrical conductivity of a T761 treated Al-Zn-Mg-Cu alloy thin plate, Mater. Res. Express. 5 (2018) 016521. https://doi.org/10.1088/2053-1591/aaa605.

[14] H. Su, H. Toda, K. Shimizu, K. Uesugi, A. Takeuchi, Y. Watanabe, Assessment of hydrogen embrittlement via image-based techniques in Al–Zn–Mg–Cu aluminum alloys, Acta Mater. 176 (2019) 96–108. https://doi.org/10.1016/j.actamat.2019.06.056.

[15] M.E. Stroe, Hydrogen embrittlement of ferrous materials, Université Libre de Bruxelles, 2006. https://doi.org/10.1016/j.corsci.2006.02.011.

[16] H.K. Birnbaum, C. Buckley, F. Zeides, E. Sirois, P. Rozenak, S. Spooner, J.S. Lin, Hydrogen in aluminum, J. Alloys Compd. 253–254 (1997) 260–264. https://doi.org/10.1016/S0925-8388(96)02968-4.

[17] G.M. Pressouyre, A classification of hydrogen traps in steel, Metall. Trans. A. 10 (1979) 1571–1573. https://doi.org/10.1007/BF02812023.

[18] H. Kamoutsi, G.N. Haidemenopoulos, V. Bontozoglou, P. V Petroyiannis, S.G. Pantelakis, Effect of prior deformation and heat treatment on the corrosion-induced hydrogen trapping in aluminium alloy 2024, Corros. Sci. 80 (2014) 139–142. https://doi.org/10.1016/j.corsci.2013.11.021.

[19] G.A. Young, J.R. Scully, The diffusion and trapping of hydrogen in high purity aluminum, Acta Metall. 18 (1998) 6337–6349. https://doi.org/10.1016/0001-6160(70)90078-7.

[20] M.O. Speidel, Hydrogen Embrittlement, in: A.R. Troiano, R. Gibala, R.F. Hehemann (Eds.), Hydrog. Embrittlement Stress Corros. Crack., 1984: pp. 271–296.

[21] J.K. Park, A.J. Ardell, Precipitation at grain boundaries in the commercial alloy Al 7075, Acta Metall. 34 (1986) 2399–2409. https://doi.org/10.1016/0001-6160(86)90143-4.

[22] N. Ben Ali, Caractérisation et modélisation micromécanique de la propagation de fissures fragiles par effet de l'hydrogène dans les alliages AA7xxx, 2011.

[23] S. Krishnanunni, R.K. Gupta, G. Ajithkumar, V. Anil Kumar, R. Ghosh, Investigation on effect of optimized RRA in strength and SCC resistance for aluminium alloy AA7010, Mater. Today Proc. 27 (2019) 2385–2389. https://doi.org/10.1016/j.matpr.2019.09.136.

[24] A.S. El-Amoush, An investigation of hydrogen-induced hardening in 7075-T6 aluminum alloy, J. Alloys Compd. 465 (2008) 497–501. https://doi.org/10.1016/j.jallcom.2007.10.126.

[25] L. Oger, M.C. Lafouresse, G. Odemer, L. Peguet, C. Blanc, Hydrogen diffusion and trapping in a low copper 7xxx aluminium alloy investigated by Scanning Kelvin Probe Force Microscopy, Mater. Sci. Eng. A. 706 (2017) 126–135. https://doi.org/10.1016/j.msea.2017.08.119.

[26] A.R. Troiano, The role of hydrogen and other interstitials in the mechanical behaviour of metals, Trans. ASM. 52 (1960) 54–80.

[27] N. Ben Ali, R. Estevez, D. Tanguy, Heterogeneity of grain boundaries in 5xxx and 7xxx aluminum alloys and its influence on intergranular toughness, Eng. Fract. Mech. 97 (2012) 1–11. https://doi.org/10.1016/j.engfracmech.2012.10.015.

[28] A.C. Umamaheshwer Rao, V. Vasu, M. Govindaraju, K.V. Sai Srinadh, Stress corrosion cracking behaviour of 7xxx aluminum alloys: A literature review, Trans. Nonferrous Met. Soc. China (English Ed. 26 (2016) 1447–1471. https://doi.org/10.1016/S1003-6326(16)64220-6.

[29] S.P. Lynch, Comments on “A unified model of environment-assisted cracking,” Scr. Mater. 61 (2009) 331–334. https://doi.org/10.1016/j.scriptamat.2009.02.031.

[30] G.M. Bond, I.M. Robertson, H.K. Birnbaum, The influence of hydrogen on deformation and fracture processes in high-strength aluminum alloys, Acta Metall. 35 (1987) 2289–2296. https://doi.org/10.1016/0001-6160(87)90076-9.

[31] I.M. Robertson, T. Tabata, W. Wei, F. Heubaum, H.K. Birnbaum, Hydrogen Embrittlement and Grain Boundary Fracture, Scr. Metall. 18 (1984) 841–846. https://doi.org/http://dx.doi.org/10.1016/0036-9748(84)90407-1.

[32] P.J. Ferreira, I.M. Robertson, H.K. Birnbaum, Hydrogen effects on the interaction between dislocations, Acta Mater. 46 (1998) 1749–1757. https://doi.org/10.1016/S1359-6454(97)00349-2.

[33] L. Oger, B. Malard, G. Odemer, L. Peguet, C. Blanc, Influence of dislocations on hydrogen diffusion and trapping in an Al-Zn-Mg aluminium alloy, Mater. Des. 180 (2019) 107901. https://doi.org/10.1016/j.matdes.2019.107901.

[34] L. Oger, E. Andrieu, G. Odemer, L. Peguet, C. Blanc, Hydrogen - dislocation interactions in a low-copper 7xxx aluminium alloy: About the analysis of interrupted stress corrosion cracking tests, Mater. Sci. Eng. A. 790 (2020) 139654. https://doi.org/10.1016/j.msea.2020.139654.

[35] M.O. Speidel, Stress corrosion cracking of aluminum alloys, Metall. Trans. A, 6 (1975) 631–651. Doi: 10.1007/BF02672284.

[36] C.E. Buckley, H.K. Birnbaum, Characterization of the charging techniques used to introduce hydrogen in aluminum, J. Alloys Compd. 330–332 (2002) 649–653. https://doi.org/10.1016/S0925-8388(01)01496-7.

[37] M.C. Lafouresse, M.-L. de Bonfils-Lahovary, C. Charvillat, L. Oger, L. Laffont, C. Blanc, A Kelvin probe force microscopy study of hydrogen insertion and desorption into 2024 aluminum alloy, J. Alloys Compd. 722 (2017) 760–766. https://doi.org/10.1016/j.jallcom.2017.06.143.

[38] C. Senöz, S. Evers, M. Stratmann, M. Rohwerder, Scanning Kelvin Probe as a highly sensitive tool for detecting hydrogen permeation with high local resolution, Electrochem. Commun. 13 (2011) 1542–1545. https://doi.org/10.1016/j.elecom.2011.10.014.

[39] E. Tohme, V. Barnier, F. Christien, C. Bosch, K. Wolski, M. Zamanzade, SKPFM study of hydrogen in a two phase material. Experiments and modelling, Int. J. Hydrogen Energy. 44 (2019) 18597–18605. https://doi.org/10.1016/j.ijhydene.2019.05.177.

[40] Z. Ma, X. Xiong, L. Chen, Y. Su, Quantitative calibration of the relationship between Volta potential measured by scanning Kelvin probe force microscope (SKPFM) and hydrogen concentration, Electrochim. Acta. 366 (2021) 137422. https://doi.org/10.1016/j.electacta.2020.137422.

[41] M. Stratmann, H. Streckel, On the atmospheric corrosion of metals which are covered with thin electrolyte layers—I. Verification of the experimental technique, Corros. Sci. 30 (1990) 681–696. https://doi.org/10.1016/0010-938X(90)90032-Z.

[42] S. Evers, C. Senöz, M. Rohwerder, Spatially resolved high sensitive measurement of hydrogen permeation by scanning Kelvin probe microscopy, Electrochim. Acta. 110 (2013) 534–538. https://doi.org/10.1016/j.electacta.2013.04.171.

[43] M.A. Krishnan, V.S. Raja, Development of high strength AA 7010 aluminum alloy resistant to environmentally assisted cracking, Corros. Sci. 109 (2016) 94–100. https://doi.org/10.1016/j.corsci.2016.03.025.

[44] S. Chen, K. Chen, P. Dong, S. Ye, L. Huang, Effect of heat treatment on stress corrosion cracking, fracture toughness and strength of 7085 aluminum alloy, Trans. Nonferrous Met. Soc. China. 24 (2014) 2320–2325. https://doi.org/10.1016/S1003-6326(14)63351-3.

[45] D. Dumont, Relations Microstructure / Ténacité dans les alliages aéronautiques de la série 7000, Institut National Polytechnique de Grenoble, 2001.

[46] Q. Puydt, Comportement mécanique de soudures en alliage d'aluminium de la série 7xxx : de la microstructure à la modélisation de la rupture, 2012.

[47] J. Deleume, Facteurs métallurgiques et mécaniques contrôlant l'amorçage de défauts de corrosion sous contrainte dans l'alliage 718 en milieu primaire des réacteurs à eau sous pression, Institut National Polytechnique de Toulouse, 2007.

[48] N. Birbilis, R.G. Buchheit, Electrochemical Characteristics of Intermetallic Phases in Aluminum Alloys, J. Electrochem. Soc. 152 (2005) B140.

[49] A. Cassell, Durability of Lean 7xxx Series Aluminium Alloys, (2013) 1–345.

[50] M. Reboul, Corrosion des alliages d'aluminium, Tech. Ingénieur. 33 (2012) 0–19.

[51] P.K. Rout, M.M. Ghosh, K.S. Ghosh, Microstructural, mechanical and electrochemical behaviour of a 7017 Al-Zn-Mg alloy of different tempers, Mater. Charact. 104 (2015) 49–60. https://doi.org/10.1016/j.matchar.2015.03.025.

[52] C. Altenbach, C. Schnatterer, U.A. Mercado, J.P. Suuronen, D. Zander, G. Requena, Synchrotron-based holotomography and X-ray fluorescence study on the stress corrosion cracking behavior of the peak-aged 7075 aluminum alloy, J. Alloys Compd. 817 (2020) 152722. https://doi.org/10.1016/j.jallcom.2019.152722.

[53] L. Wang, J. Liang, H. Li, L. Cheng, Z. Cui, Quantitative study of the corrosion evolution and stress corrosion cracking of high strength aluminum alloys in solution and thin electrolyte layer containing Cl-, Corros. Sci. 178 (2021) 109076. https://doi.org/10.1016/j.corsci.2020.109076.

[54] X. Qi, R. Song, W. Qi, J. Jin, C. Wang, H. Li, Y. Xiong, Consistent variation of stress corrosion cracking susceptibility and passive film-induced stress for 7050 aluminum alloy with polarization potential, Xiyou Jinshu Cailiao Yu Gongcheng/Rare Met. Mater. Eng. 45 (2016) 1943–1948. https://doi.org/10.1016/s1875-5372(16)30151-5.

[55] R.G. Song, W. Dietzel, B.J. Zhang, W.J. Liu, M.K. Tseng, A. Atrens, Stress corrosion cracking and hydrogen embrittlement of an Al-Zn-Mg-Cu alloy, Acta Mater. 52 (2004) 4727–4743. https://doi.org/10.1016/j.actamat.2004.06.023.

[56] J.M. Ducéré, M.D. Rouhani, C. Rossi, A. Estève, Role of impurities , defects and their complexes on the trapping of hydrogen in bulk aluminum and on the Al (1 1 1) surface, Comput. Mat. Sci. 126 (2017) 272–279. https://doi.org/10.1016/j.commatsci.2016.09.047.

[57] H. Kamoutsi, G.N. Haidemenopoulos, H. Mavros, C. Karantonidis, P. Floratos, Z. Alhosani, P. Cho, D.H. Anjum, F. Ravaux, K. Polychronopoulou, Effect of precipitate coherency on the corrosion-induced hydrogen trapping in 2024 aluminum alloy, Int. J. Hydrogen Energy 46 (2021) 34487–34497. https://doi.org/10.1016/j.ijhydene.2021.08.005.

[58] J. Philibert, A. Vignes, Y. Bréchet, Partie 2 : Métallurgie Physique, in: Métallurgie - Du Minerai Au Matériau, n.d.

[59] M. Ichimura, Y. Sasajima, M. Imabayashi, Grain boundary effect on diffusion of hydrogen in pure aluminum, Materials Transactions, JIM, 32 (1991) 1109–1114. https://doi.org/10.2320/matertrans1989.32.1109.

[60] A. Pedersen, H. Jónsson, Simulations of hydrogen diffusion at grain boundaries in aluminum, Acta Materialia 57 (2009) 4036–4045. https://doi:10.1016/j.actamat.2009.04.057.

[61] T. Müetschele, R. Kirchheim, Segregation and diffusion of hydrogen in grain boundaries of palladium, Scripta Metall 21 (1987) 135–140. https://doi.org/10.1016/0036-9748(87)90423-6).

[62] J. Chene, I.M. Bernstein, A.W. Thompson, Role of Heat Treatment and Cathodic Charging Conditions on the Hydrogen Embrittlement of HP 7075 Aluminum Alloy, Metallurgical Transactions A, 21a (1990) 455-464. https://doi.org/10.1007/BF02782426.

[63] H. Saitoh, Y. Iijima, K. Hirano, Behaviour of hydrogen in pure aluminium, Al-4 mass% Cu and Al-1 mass% Mg_2Si alloys studied by tritium electron microautoradiography, J. Mater. Sci. 29 (1994) 5739–5744. https://doi.org/10.1007/BF00349974.

[64] M.S. Bhuiyan, H. Toda, Z. Peng, S. Hang, K. Horikawa, K. Uesugi, A. Takeuchi, N. Sakaguchi, Y. Watanabe, Combined microtomography, thermal desorption spectroscopy, X-ray diffraction study of hydrogen trapping behavior in 7XXX aluminum alloys, Mater. Sci. Eng. A. 655 (2016) 221–228. https://doi.org/10.1016/j.msea.2015.12.092.

[65] P. Kumar Rout, K.S. Ghosh, Effect of microstructural features on stress corrosion cracking behaviour of 7017 and 7150 aluminium alloy, Mater. Today Proc. 5 (2018) 2391–2400. https://doi.org/10.1016/j.matpr.2017.11.462.

[66] P. Xie, S. Chen, K. Chen, H. Jiao, L. Huang, Z. Zhang, Z. Yang, Enhancing the stress corrosion cracking resistance of a low-Cu containing Al-Zn-Mg-Cu aluminum alloy by step-quench and aging heat treatment, Corros. Sci. 161 (2019) 108184. https://doi.org/10.1016/j.corsci.2019.108184.

[67] M. Yu, H. Zu, K. Zhao, J. Liu, S. Li, Effects of dry/wet ratio and pre-immersion on stress corrosion cracking of 7050-T7451 aluminum alloy under wet-dry cyclic conditions, Chinese J. Aeronaut. 31 (2018) 2176–2184. https://doi.org/10.1016/j.cja.2018.01.008.

[68] M. Safyari, M. Moshtaghi, S. Kuramoto, On the role of traps in the microstructural control of environmental hydrogen embrittlement of a 7xxx series aluminum alloy, J. Alloys Compd. 855 (2021) 157300. https://doi.org/10.1016/j.jallcom.2020.157300.

[69] G. Itoh, K. Koyama, M. Kanno, Evidence for the transport of impurity hydrogen with gliding dislocations in aluminum, Scr. Mater. 35 (1996) 695–698.

[70] P.J. Ferreira, I.M. Robertson, H.K. Birnbaum, Hydrogen effects on the character of dislocations in high-purity aluminum, Acta Mater. 47 (1999) 2991–2998. https://doi.org/10.1016/S1359-6454(99)00156-1.

[71] D.-G. Xie, L. Wan, Z.-W. Shan, Hydrogen enhanced cracking via dynamic formation of grain boundary inside aluminium crystal, Corros. Sci. 183 (2021) 109307. https://doi.org/https://doi.org/10.1016/j.corsci.2021.109307.

[72] L.L. Liu, Q.L. Pan, X.D. Wang, S.W. Xiong, The effects of aging treatments on mechanical property and corrosion behavior of spray formed 7055 aluminium alloy, J. Alloys Compd. 735 (2018) 261–276. https://doi.org/10.1016/j.jallcom.2017.11.070.

[73] J. Chen, X. Zhang, L. Zou, Y. Yu, Q. Li, Effect of precipitate state on the stress corrosion behavior of 7050 aluminum alloy, Mater. Charact. 114 (2016) 1–8. https://doi.org/10.1016/j.matchar.2016.01.022.

[74] Y.L. Wang, H.C. Jiang, Z.M. Li, D.S. Yan, D. Zhang, L.J. Rong, Two-stage double peaks ageing and its effect on stress corrosion cracking susceptibility of Al-Zn-Mg alloy, J. Mater. Sci. Technol. 34 (2018) 1250–1257. https://doi.org/10.1016/j.jmst.2017.05.008.

[75] M. Puiggali, A. Zielinski, J.M. Olive, E. Renauld, D. Desjardins, M. Cid, Effect of microsructure on stress corrosion cracking of an Al-Zn-Mg-Cu Alloy, Corros. Sci. 40 (1998) 805–819. https://doi.org/https://doi.org/10.1016/S0010-938X(98)00002-X.

[76] J.R. Scully, G.A. Young, S.W. Smith, Hydrogen embrittlement of aluminum and aluminum-based alloys, in: Gaseous Hydrog. Embrittlement Mater. Energy Technol., Elsevier, 2012: pp. 707–768. https://doi.org/10.1533/9780857093899.3.707.

[77] A.S. El-Amoush, Investigation of corrosion behaviour of hydrogenated 7075-T6 aluminum alloy, J. Alloys Compd. 443 (2007) 171–177. https://doi.org/10.1016/j.jallcom.2006.12.045.

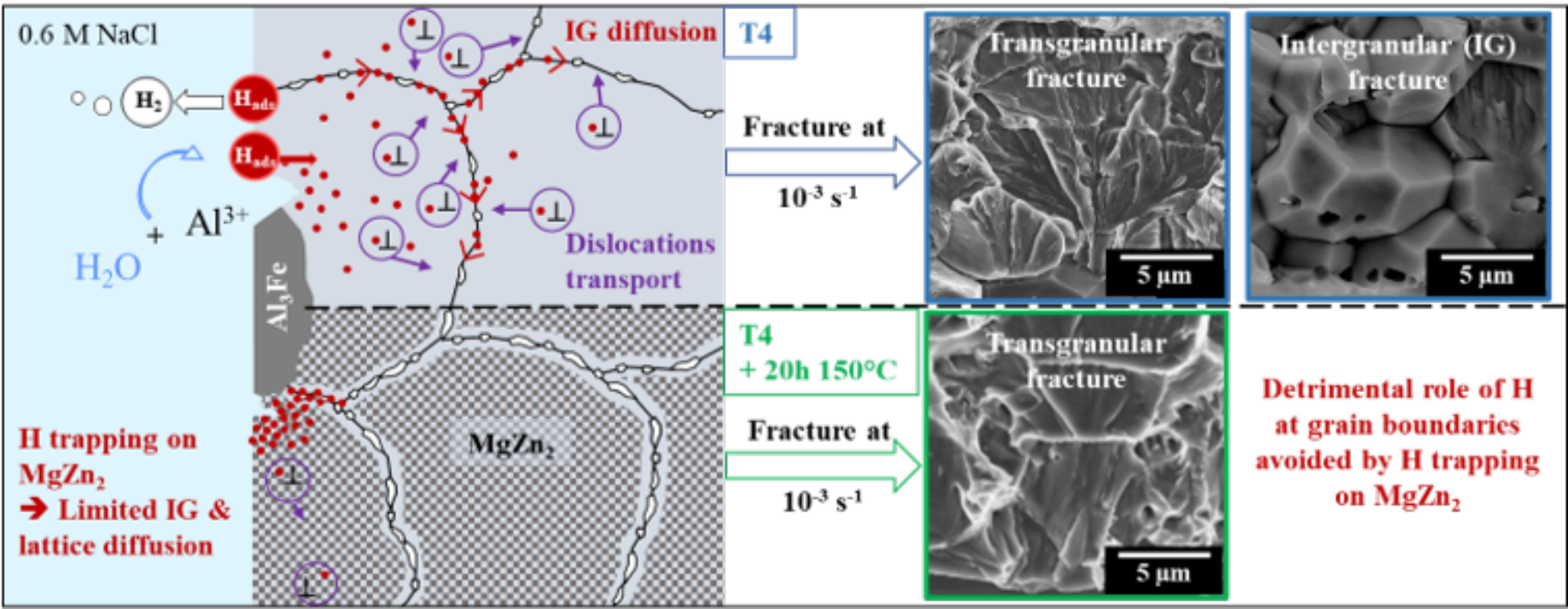
0.6 M NaCl
H_2
H_{ads}
H_{ads}
Al^{3+}
H_2O
IG diffusion
Dislocations transport
Al_3Fe
$MgZn_2$
H trapping on $MgZn_2$
➔ Limited IG & lattice diffusion
T4
Fracture at
10^{-3} s^{-1}
Transgranular fracture
5 µm
Intergranular (IG) fracture
5 µm
T4
+ 20h 150°C
Fracture at
10^{-3} s^{-1}
Transgranular fracture
5 µm
Detrimental role of H at grain boundaries avoided by H trapping on $MgZn_2$